1 **Experimental investigation on material properties and residual stresses in cold-formed high**
2 **strength steel irregular octagonal hollow sections**
3

4 Jun-zhi Liu[1], Han Fang[3], Tak-Ming Chan[1, 2, *]
5

6 1 Department of Civil and Environmental Engineering, The Hong Kong Polytechnic University, Hong Kong, China

7 2 Chinese National Engineering Research Centre for Steel Construction (Hong Kong Branch), The Hong Kong Polytechnic

8 University, Hong Kong, China

9 3 School of Civil, Environmental and Mining Engineering, The University of Adelaide, South Australia 5005, Australia

10 * Corresponding author: tak-ming.chan@polyu.edu.hk

11

12 **Abstract**

13

14 A systematic investigation into the variation of the material properties and residual stress distribution across
15 cold-formed high strength steel (HSS) irregular octagonal hollow sections (IOctHS) is presented in this paper.
16 The specimens were fabricated through welding the two cold-formed half-sections by gas metal arc welding
17 (GMAW). Non-destructive inspection was executed to detect any cracks in the welding internally and
18 externally. Tensile tests on coupon specimens taken from the critical locations within the cross sections were
19 carried out to measure the material properties variation within the HSS IOctHS. The material strength
20 variations within different cross sections exhibit an anticipated similar pattern that strength enhancement at
21 corner regions was more obvious than flat coupons counterpart. The largest strength enhancement is 8.4%
22 at corner region compared with the average yield strength of parent plates, whereas the yield strength and
23 ultimate strength of flat coupon specimens generally fluctuate at a certain level. Based on the obtained
24 material properties, the existing material models for predicting the stress-strain curves were assessed and
25 new material models are proposed to generate the stress-strain relationship for materials within the HSS
26 IOctHS. Moreover, the residual stress measurement for cold-formed HSS IOctHS was performed using the
27 sectioning method. A total of 55 strip specimens were extracted from the cross sections of HSS IOctHS with
28 more than 660 strain readings. Based on the residual stress measurement results, the magnitude and
29 distribution pattern of the residual stresses are presented and discussed. A predictive model for residual stress
30 distribution of the cold-formed HSS IOctHS was developed.
31

32 **Keywords:** High strength steel; Cold-formed; Material properties; Residual stress; Irregular Octagonal
33 sections

34

35 **1. Introduction**

36

37 With the recent manufacturing development and advancement of the high strength steel materials, high
38 strength steel (HSS) tubular structures provide combined advantages of structural efficiency, high strength-
39 to-weight ratio as well as the low carbon footprint for lower environmental impacts. These merits inherently
40 prompt the research exploration of the HSS material properties and structural performance of HSS tubular
41 structures for their application in construction [1–2]. Numerous investigations have been carried out for local
42 buckling behaviour of HSS tubular structures with various cross-sectional shapes including square hollow
43 sections (SHS), rectangular hollow sections (RHS), circular hollow sections (CHS) and elliptical hollow
44 sections (EHS) [3–10]. In recent years, the application of the polygonal tubular sections is gaining increasing

45   interests [11–14]. In the polygonal section family, octagonal hollow sections (OctHS), characterized with

46   relative higher local buckling resistance than that of SHS or RHS counterparts and facilitated the

47   construction of beam-column connections compared with CHS counterparts, have gained increasing

48   popularity and attention [15–19]. OctHS members become attractive options for architects and structural

49   engineers and have been utilized in civil structural applications including electricity transmission line

50   structures, lattice structures in antennas as well as lighting structures [20– 21], as depicted in Fig. 1.

51   Systematic research has been carried out to examine the structural performance of OctHS experimentally

52   [17, 18, 22, 23] and numerically [16, 24, 25]. Kabanda and MacDougall [14] illustrated that increasing the

53   depth of the polygonal sections will improve the bending stiffness. Hence, irregular octagonal sections

54   (IOctHS) with increased depth of the web of the OctHS becomes a solution to increase the major-axis

55   stiffness of the cross section in bending and provide large connection area for the incoming members.

56   However, no experimental investigation has been carried out for IOctHS with different aspect ratios.

57

58   Distinct from the built-up tubular sections which simply contain welding fabrication process, cold-formed

59   tubular sections are characterized with the combined processes of press-braking or cold-rolling and welding.

60   These fabrication processes can affect material properties within the IOctHS. For example, in the region near

61   the welding seam, the material properties within the heat affected zone (HAZ) are different from those

62   outside HAZ due to the changes in micro-structures. Reduction in yield strength and ultimate strength can

63   be observed linearly proportional to the line heat input [26–27]. Moreover, cold-forming process of press-

64   braking exceedingly results in plastic deformation at corner regions associated with strain hardening, by

65   which the yield strength and ultimate strength can be enhanced [61]. In addition to the material properties

66   variation, the residual stresses can also be generated due to the fabrication processes of press-braking and

67   welding, resulting in premature failure of the structural members. The measurement of residual stresses for

68   HSS cold-formed sections have been carried out in past years focusing on circular (CHSs), square (SHSs)

69   and rectangular (RHSs) hollow sections [1, 28]. Experimental studies of residual stress measurement for

70   HSS OctHS with nominal yield strength of 690 MPa have been conducted by Fang et al. [29] and those with

71   nominal yield strength of 460 MPa was carried out by Chen et al. [19]. No experimental investigations for

72   residual stress measurement have been carried out for HSS IOctHS.

73

74   Hence, the material properties variation and residual stresses of cold-formed HSS IOctHS manufactured

75   from HSS plates with nominal yield strength of 690 MPa were studied in this paper. Tensile coupon tests

76   were carried out to examine the material properties variation with coupon specimens taken from the critical

77   locations within the cross sections. Suitable material models for the materials at flat and corner portions were

78   assessed and developed. Experimental investigations on residual stresses were also carried out for four HSS

79   cold-formed IOctHS with two different nominal thicknesses of 6 mm and 10 mm and nominal aspect ratios

80   of 1.5 and 2.0. To implement the sectioning method, the strips from the cross sections were cut by a wire-

81   cutting machine. A total of 55 strip test specimens was extracted from the cross section of HSS IOctHS with

82   more than 660 strain readings recorded. Based on the experimental results, the magnitude and distribution

83   pattern of the residual stresses are presented and discussed. A predictive model for residual stress distribution

84   within the cold-formed HSS IOctHS was developed.

85

86   **2. HSS cold-formed irregular octagonal hollow section specimens**

87

88   HSS steel plates with nominal thicknesses of 6 mm and 10 mm and delivered in Quenched and Tempered

89　(QT) conditions were used to fabricate the cold-formed IOctHS. The chemical compositions of the HSS
90　plates are given in Table. 1. For the fabrication of the specimens, firstly, the cold-forming process of press-
91　braking was performed at room temperature with the HSS plates folded longitudinally. Subsequently, the
92　two cold-formed half-sections were longitudinally welded by gas metal arc welding (GMAW). The ceramic
93　material was filled as backing materials prior to the implementation of multiple welding passes. To have an
94　over-matched welding condition, 1.2 mm electrode of ER110S-G category (f_y = 860 MPa, f_u = 920 MPa)
95　was selected with chemical compositions provided in Table. 2.
96
97　The geometry of the fabricated HSS cold-formed IOctHS was labelled using the nomenclature presented in
98　Fig. 2. The nominal dimensions of HSS cold-formed IOctHS are (B_L× t × aspect ratio) 145 × 6-1.50, 220 ×
99　6-1.50 and 225 × 6-2.00 and 145×10-1.50 respectively. In Fig. 3, the nomenclature of B_s, b_s B_L, b_L, t, and r_i
100　represent the short edge length, inclined short length, long edge length, long flat portion side length,
101　thickness, and the inner corner radius whereas the aspect ratio is defined as H/B. The measured dimensions
102　of the IOctHS specimens are summarized in Table. 3. The specimens were labelled in a form of "IOctHS-
103　nominal edge length B_L × thickness-aspect ratio". Taking specimen of IOctHS225×6-2.00 as an example,
104　the label represents that the specimen was fabricated with nominal B_L of 225 mm, nominal t of 6 mm and an
105　aspect ratio of 2.0. The examined HSS IOctHS specimens cover a large spectrum of cross section slenderness
106　with plate width-to-thickness ratios ranging between 3.7 and 34.7. Prior to testing, the X-ray inspection
107　depicted in Fig. 4 was conducted in accordance with the specification of ISO 17636-1 [30]. Welding defects
108　including crack, porosity and undercut were not observed. The external surfaces of the corner region and the
109　longitudinal welding were also attested by magnetic particle inspection to ensure that no crack was caused
110　subject to large plastic deformation. The inspection for the surface crack of welding is illustrated in Fig. 5.
111　Based on the contrast paint and the particle aerosol, the crack can be inspected clearly based on the magnetic
112　field generated by the electromagnetic yoke. No crack was found on the external surface of the corner regions
113　and welding surfaces.
114
3. Material properties investigations

3.1. Tensile coupon specimens

119　The tensile coupon specimens were cut from both the parent HSS plates and the HSS cold-formed IOctHS.
120　Six tensile coupon specimens were longitudinally and transversely taken from the parent plates with different
121　thicknesses. Alongside with the parent plate coupon specimens, the coupon specimens, namely flat coupons,
122　and corner coupons respectively, were also machined from the flat and corner portions of the HSS IOctHS
123　to examine the effect of press-braking. In order to examine the material variation across the cross section of
124　HSS IOctHS, flat and corner coupon specimens were also taken from different locations across the quarter-
125　section of the HSS IOctHS by assuming that the material properties were symmetrically distributed due to
126　the dual-symmetrical geometries. Moreover, the coupon specimens at the welding seam for each IOctHS
127　were also extracted to examine any effect within the HAZ.
128
129　Nominal dimensions for the parent plate-, flat- and corner coupon specimens are designed as per ISO EN
130　6892-1: 2019 [31]and shown in Figs. 6–8. Width of 13 mm and 8 mm along the parallel gauge length
131　respectively was designed for specimens extracted from 6 mm and 10 mm thick plates for parent coupons,
132　as presented in Fig. 6. For flat coupons and corner coupon specimens, they were machined with 4 mm and

8 mm width along the gauge length for those from the sections with plate thicknesses of 6 mm and 10 mm respectively. The detailed dimensions of the flat coupon specimens are depicted in Fig. 7. Note that for corner specimen, two holes with diameter of 10 mm were drilled at the distance of 20 mm from the end of the couponto avoid the net failure at the end of the coupon specimen near the holes. The tensile loading was applied to each corner coupon specimen through a pair of specially developed grips with two pins through its centroid, as shown in Fig. 9(b).

The locations for the tensile coupon specimens across different HSS cold-formed IOctHS are depicted in Figs. 10–13. These coupon specimens were labelled in a similar way to that for the IOctHS with the addition of the location where the coupon specimens were extracted. For example, IOctHS145×6-1.50-F4 stands for a flat coupon specimen cut from the HSS IOctHS145×6-1.50 at the location labelled as F4 shown in Fig. 10. Prior to testing, the actual dimensions of the flat coupon specimens were measured using a digital Vernier caliper whereas for the corner coupons, the Mitutoyo digital micrometer with flat spindle was used. The cross-section area of the corner coupon specimens was determined by using CAD scanning method as introduced in [32, 33].

3.2. Test procedures

An INSTRON in-house 5982 electro-mechanical high force universal testing system with a capacity of 100 kN was used to conduct the tensile coupon tests, as shown in Fig. 9. An optical non-contact video extensometer with a gauge length of either 25 mm or 50 mm painted by white dots was used to capture the full engineering stress-strain relationship. The elongation at fracture for the gauge length of either 25 mm ($\varepsilon_{f,25}$) or 50 mm ($\varepsilon_{f,50}$) can be directly obtained via the video extensometer. As for the coupons failed outside the effective gauge length range of the video extensometer, it was determined by carefully fitting the fractured pieces and comparing the final gauge length to the original gauge length. According to the EN ISO 6892-1:2019 [31], the proportional elongation at fracture (ε_f) is obtained based on an original gauge length of $5.65\sqrt{A}$, where A is cross-sectional area along the parallel original gauge length of the coupon. Four strain gauges were affixed to the mid-length on both sides of each coupon to determine Poisson's ratio and modulus for parent coupons whereas two strain gauges were adhered to flat and corner coupons to measure the elastic modulus. The key averaged measured material properties for parent plate coupons are summarized in Table. 4, where E_s indicates the elastic modulus, f_y is yield strength for steel with yield plateau or 0.02% proof stress, $f_{0.05}$ is the 0.05% proof stress, n is the strain hardening component, f_u is the ultimate strength, ε_{sh} is strain-hardening strain, ε_u is strain at ultimate strength, ε_f is the proportional elongation at fracture. A letter "p" in the subscript indicates that the results are obtained for the parent plates. The distribution and magnitudes of the yield strength and ultimate strength measured for the coupon specimens within the sections are plotted against the corresponding extracted locations with labeling, as shown in Figs. 10–13. The measured material properties are also summarized in Tables 5–8.

3.4. Test results and discussions

All the tensile coupon specimens were featured with fracture failure in the middle of the parallel gauge length. The flat tensile coupon specimens featured with larger strains of elongation at fracture than those observed for corner coupons. Besides, the ratio of the ultimate strength to the yield strength should be greater than 1.05 with elongation strain at failure greater than 10% and 15 times the yield strain for the steels with

177 nominal yield strength higher than 460 MPa, as specified in EN 1993-1-12 [34]. All the flat tensile coupon
178 specimens meet the specifications codified in EN 1993-1-12 [34]. The corner coupon specimens cannot meet
179 the requirement of the ratio of ultimate strain over yield strain with average $\varepsilon_u/\varepsilon_y$ smaller than 5. The reduced
180 ductility for the corner coupons is primarily attributed to the large plastic deformation experienced during
181 the press-braking fabrication. Based on the comparisons between the yield strength and ultimate strength
182 variations for each IOctHS in Figs. 10–13, the variation pattern of the material properties for HSS IOctHS
183 generally exhibit consistent characteristics with yield strength and ultimate strength improved at corner
184 regions. Relatively lower yield strength is observed for the tensile coupon specimens taken from the welding
185 seam. Its softening modulus resulted in lower 0.02% proof stress compared with that of flat coupons. The
186 graphs of strength distribution within the sections also demonstrate that the variation of the material
187 properties is independent of the aspect ratio.
188
189 Compared with the average yield strength of the parent plate, flat coupon specimens demonstrate strength
190 enhancement of 1.3%, 1.7%, 2.1% and 5.2% based on averaged tested yield strength for sections of
191 IOctHS145×6-1.50, IOctHS220×6-1.50, IOctHS225×6-2.00 and IOctHS145×10-1.50 respectively. An
192 increased value of 1.7%, 1.6%, and 2.5% was observed for ultimate strength of IOctHS145×6-1.50,
193 IOctHS220×6-1.50, IOctHS225×6-2.00 sections, compared with the averaged ultimate strength from parent
194 plate. The improvement of ultimate strength for flat coupons adjacent to the corners from the IOctHS145×10-
195 1.50 section is 5.6% and higher than that observed for other sections. The strength improvement for the
196 corner coupons in terms of the yield strength in comparison with that of flat coupons was 7.5%, 4.4% 7.4%
197 and 8.4% on average and the ultimate strength increased with 6.2%, 5.9%, 7.3% and
198 9.4% respectively for IOctHS145×6-1.50, IOctHS220×6-1.50, IOctHS225×6-2.00 and IOctHS145×10-1.50
199 sections.
200
201 **3.5. Development of stress-strain model for HSS IOctHS**
202
203 The material stress-strain relationship is indispensable for the analysis and design of HSS IOctHS structures.
204 It should be noted that the stress-strain responses of the coupon specimens from HSS IOctHS investigated
205 in this study exhibit two kinds of patterns. The stress-strain curves from the cross sections with 10 mm thick
206 steel plates mainly display moderate level of strain-hardening with obvious yield plateau whereas the
207 sections comprising 6 mm steel plates mainly display a relatively rounded response. The conventional multi-
208 linear model for hot-rolled steel is inappropriate for these responses as the gradual decreased hardening
209 stiffness cannot be captured and may lead to inaccurate design and analysis. Hence, accurate material models
210 to describe these stress-strain features need to be developed.
211
212 **3.5.1. Stress-strain model for coupon specimens with rounded stress-strain response**
213 **3.5.1.1. Existing stress-strain models**
214
215 To develop the stress-strain model for the steel material with rounded responses, researchers have carried
216 out numerous investigations to generate the suitable model applicable to those materials. It should be noted
217 that all these models were developed based on the fundamental form known as Ramberg-Osgood (R-O)
218 model. Various stress-strain models were evolved and improved based on this simple form with additions of
219 strain hardening parameters to account for the non-linear pattern of the stress-strain curve or removals of
220 strain component for simplicity. The brief introduction on the development of the non-linear stress-strain

221   models is presented below.

222

223   To predict the stress-strain relationship for cold-formed carbon or stainless steel and foster the generic model,

224   Ramberg-Osgood (R-O) relationship was considered as the most commonly used model as shown in Eq. (1).

225
$$\varepsilon = \frac{\sigma}{E_{s}} + p\left(\frac{\sigma}{f_{p}}\right)^{n} \quad \text{for } 0 \le \sigma \le f_{u} \tag{1}$$

226

227   where σ indicates the stress and ε denotes the strain, E_{s} is the elastic modulus, f_{p} is the proof stress

228   corresponds to the stress at plastic strain p, n is the exponent component to describe the degree of the

229   curvature of the stress strain response. The R-O model was developed by Hill [35] with modifications to the

230   plastic strain with 0.002 and stress with 0.2% proof strength which can provide accurate stress-strain curve

231   up to the point of 0.2% proof strength, a commonly adopted proof strength for non-linear stress-strain

232   relationship of metallic materials. However, the predictions based on 0.2% plastic strain are not able to

233   provide accurate stress-strain path after the 0.2% proof strength. To overcome the limitations in the stress-

234   strain model proposed by Hill [35], Mirambell and Real [36] proposed a two-stage R-O model based on

235   validation against a series of coupon tests of stainless-steel materials with a new exponential component m

236   describing the non-linear strain hardening level of stress-strain curves after reaching the 0.2% proof strength,

237   as follows

238

239
$$\varepsilon = \frac{\sigma - f_{0.2}}{E_{0.2}} + \varepsilon_{pu}\left(\frac{\sigma - f_{0.2}}{f_{u} - f_{0.2}}\right)^{m} + \varepsilon_{0.2} \quad \text{for} \quad f_{0.2} \le \sigma \le f_{u} \tag{2}$$

240

241   where $E_{0.2}$ is the tangent modulus at $f_{0.2}$, $\varepsilon_{0.2}$ is the total strain at the 0.2% proof strength, ε_{pl} is the plastic

242   strain corresponding to the ultimate strength.

243   Rasmussen [37] further proposed a simplified expression to describe the stress-strain response based on the

244   assumption that the difference between the plastic strain and the total strain at the ultimate strength is

245   negligible. Hence, the expression in Eq. (2) is expressed with a simple parameter ε_{u} in Eq. (3) instead of the

246   plastic strain in Eq. (2) as the total strain can be directly obtained from the experimental stress-strain curve.

247

248
$$\varepsilon = \frac{\sigma - f_{0.2}}{E_{0.2}} + \varepsilon_{u}\left(\frac{\sigma - f_{0.2}}{f_{u} - f_{0.2}}\right)^{m} + \varepsilon_{0.2} \quad \text{for} \quad f_{0.2} \le \sigma \le f_{u} \tag{3}$$

249

250   To develop a generic and precise stress-strain model applicable for cold-formed carbon steels, which can

251   accurately represent the curve up to the ultimate strength without overly predicted yield strength, Gardner

252   and Yun [38] collected experimental stress-strain curves from existing investigations. A model was

253   subsequently proposed applicable for cold-formed carbon steel precisely based on the six given material

254   properties from the tensile coupon tests, including $f_{0.2}$, $\varepsilon_{0.2}$, f_{u}, $E_{0.2}$, $f_{0.05}$, and n.

255

256
$$\varepsilon = \begin{cases} \dfrac{\sigma}{E_s} + 0.002\left(\dfrac{\sigma}{f_{0.2}}\right)^n & \text{for } \sigma \le \sigma_{0.2} \\[4mm] \dfrac{\sigma - f_{0.2}}{E_{0.2}} + \left(\varepsilon_u - \varepsilon_{0.2} - \dfrac{f_u - f_{0.2}}{E_{0.2}}\right)\left(\dfrac{\sigma - f_{0.2}}{f_u - f_{0.2}}\right)^m + \varepsilon_{0.2} & \text{for } \sigma > \sigma_{0.2} \end{cases} \qquad (4)$$

257 where the exponent m and the tangent modulus $E_{0.2}$ can be derived based on the follows,

258
$$m = 1 + 3.3\left(\frac{f_{0.2}}{f_u}\right) \qquad (5)$$

259
$$E_{0.2} = \frac{E_s}{1 + 0.002nE_s / f_{0.2}} \qquad (6)$$

260
261 or alternatively obtained from the following with the proof 1.0% stress needed,
262

263
$$m = \frac{\ln\left(0.008 + \dfrac{f_{1.0} - f_{0.2}}{E} - \dfrac{f_{1.0} - f_{0.2}}{E_{0.2}}\right) - \ln\left(\varepsilon_u - \varepsilon_{0.2} - \dfrac{f_u - f_{0.2}}{E_{0.2}}\right)}{\ln(f_{1.0} - f_{0.2}) - \ln(f_u - f_{0.2})} \qquad (7)$$

264
265 Moreover, Arrayago et al. [39] and Gardner and Yun [38] concluded that using 0.05% proof strength instead
266 of 0.01% proof strength yields increased accuracy and consistency. Thus, the first stage hardening
267 component n was determined as follows, in Eq. (8)
268

269
$$n = \frac{\ln(4)}{\ln(f_y / f_{0.05})} \qquad (8)$$

270 For the purpose of easy application, Abdella [40] also provided the inversion form of the stress-strain model
271 for Eq. (4), by which the stress is expressed in terms of strain, as follows in Eqs. (9) – (11).
272

273
$$f_n = \begin{cases} \dfrac{r\varepsilon_n}{1 + (r-1)\varepsilon_n^p} & \text{for } 0 \le \varepsilon_n < 1 \\[4mm] 1 + \dfrac{r_{0.2}(\varepsilon_n - 1)}{1 + (r^* - 1)\left(\dfrac{\varepsilon_n - 1}{\varepsilon_{nu} - 1}\right)^{p^*}} & \text{for } 1 \le \varepsilon_n < \varepsilon_{nu} \end{cases} \qquad (9)$$

274 where the related parameters of r^* and p^* can be determined following Eq. (10) and Eq. (11).

275
$$p^* = r^* \frac{1 - r_u}{r^* - 1} \qquad (10)$$

276
$$r^* = \frac{E_{0.2}(\varepsilon_u - \varepsilon_{0.2})}{f_u - f_{0.2}} \qquad (11)$$

277 f_n is the stress in a normalized form with $f_{0.2}$ ($f_n = \sigma/f_{0.2}$), ε_n is the normalized strain by $\varepsilon_{0.2}$ ($\varepsilon_n = \varepsilon/\varepsilon_{0.2}$), ε_{nu} is
278 the normalized strain corresponding to the ultimate strength ($\varepsilon_{nu} = \varepsilon_u/\varepsilon_{0.2}$), $r = E\varepsilon_{0.2}/f_{0.2}$, $r_{0.2} = E_{0.2}\varepsilon_{0.2}/f_{0.2}$, r_u
279 $= E_u(\varepsilon_u - \varepsilon_{0.2})/(f_u - f_{0.2})$, $E_u = E_{0.2}/(1 + (r^* - 1)m)$.
280

281 It should be noted that analogous to the inversion form of R-O model proposed in [40], the Hopperstad
282 exponential stress-strain model also specifies the uniaxial stress-strain behaviour in the form of $\sigma = \sigma(\varepsilon)$
283 which is commonly used and suitable for implementation in numerical model to describe the material
284 behaviour [64]. The Hopperstad model used two material constants A and B to describe the strain hardening
285 and shape of the curve. As Hopperstad model is not used to construct the material model of HSS IOctHS
286 investaged in this study, detailed discussions will not be further carried out.
287

288 Moreover, investigations have also been carried out to formulate the stress-strain model with reduced
289 material parameters. Based on two-stage R-O model, a generic multi-stage model was proposed by Hradil
290 et al. [41], which decomposes the stress-strain curve into segments with intermediate points. The multi-stage
291 model is a unified approach which simplifies the processing of material data. Fig. 14 illustrates the schematic
292 view of the multi-stage stress-strain model. The stress-strain curve comprises four stages namely stage I to
293 stage IV. Each stage of the stress-strain curve can be described using the tangent modulus of elasticity E_i,
294 stress f_n and plastic strain ε_{pl}, as follows, in Eqs. (12) – (14).
295

296 $$\varepsilon = \frac{\sigma - f_i}{E_i} + \varepsilon_i^* \left(\frac{\sigma - f_i}{\Delta f_i} \right)^m + \varepsilon_i^{pl} + \frac{f_i}{E_0} \quad \text{for} \quad f_i \le \sigma \le f_{i+1} \tag{12}$$

297 where

298 $$E_{i+1} = \frac{E_i}{1 + \varepsilon_i^* n_i (E_i / \Delta f_i)} \tag{13}$$

299 $$\varepsilon_i^* = \Delta \varepsilon_i^{pl} - \Delta f_i \left(\frac{1}{E_i} - \frac{1}{E_0} \right) \tag{14}$$

300 where $\Delta\varepsilon_i^{pl} = \varepsilon_{i+1}^{pl} - \varepsilon_i^{pl}$ and $\Delta f_i = f_{i+1} - f_i$, while the stress f_{i+1} should meet the consecutive relation with
301 $f_i < f_{i+1} \le f_i + \Delta\varepsilon_i^{pl} (E_0 E_i)/(E_0 - E_i)$.
302

303 Inspired by the Abdella's [40] work, the inversion form of the multi-stage stress-strain model was provided
304 by Hradil et al. [41]. For the purpose of easy application, a three-stage stress-strain model was proposed, as
305 given in Eqs. (15) – (18). This three-stage stress-strain model is later compared with the experimental stress-
306 strain data for the flat coupon specimens taken from the cross section of HSS IOctHS. The comparisons
307 between the predictions from the Hradil's model and the experimental results from IOctHS145×6-150-F4
308 are illustrated in Fig. 16. The detailed comparisons and discussions between these predictions from various
309 stress-strain models are provided in section 3.5.1.2.
310

311
$$\varepsilon = \begin{cases} \dfrac{\sigma}{E_s} + 0.002\left(\dfrac{\sigma}{f_{0.2}}\right)^{n_{0-0.2}} & \text{for } \sigma \leq f_{0.2} \\[4mm] \dfrac{\sigma - f_{0.2}}{E_{0.2}} + \varepsilon_{0.2}^{*}\left(\dfrac{\sigma - f_{0.2}}{f_{1.0} - f_{0.2}}\right)^{n_{0.2-1.0}} + 0.002 + \dfrac{f_{0.2}}{E_s} & \text{for } f_{0.2} < \sigma \leq f_{1.0} \\[4mm] \dfrac{\sigma - f_{1.0}}{E_{1.0}} + \varepsilon_{1.0}^{*}\left(\dfrac{\sigma - f_{1.0}}{f_u - f_{1.0}}\right)^{n_{1.0-u}} + 0.01 + \dfrac{f_{1.0}}{E_s} & \text{for } f_{1.0} < \sigma \leq f_u \end{cases}$$
(15)

312   where the tengent modulus of elasticity equivalent plastic strain of the second and the third stage are as
313   follows,

314
$$E_{1.0} = \frac{E_{0.2}}{1 + \varepsilon_{0.2}^{*} n_{0.2-1.0}(E_{0.2}/(\Delta f_{1.0} - f_{0.2}))}$$
(16)

315
$$\varepsilon_{0.2}^{*} = 0.008 - (f_{1.0} - f_{0.2})\left(\frac{1}{E_{0.2}} - \frac{1}{E_s}\right)$$
(17)

316
$$\varepsilon_{1.0}^{*} = (\varepsilon_u^{pl} - 0.01) - (f_u - f_{1.0})\left(\frac{1}{E_{1.0}} - \frac{1}{E_s}\right)$$
(18)

317   Following the extensive experimental investigations for HSS cold-formed structural members, a material
318   model to develop the stress-strain curves for cold-formed HSS was also proposed in Ma et al. [1]. However,
319   the iterations and lengthy expressions limit their application in engineering practice. To overcome this
320   limitation and develop the stress-strain model for HSS, Xia et al. [42] performed tensile coupon tests for
321   high strength and low-alloy steel (HSLA700) and martensitic steel (MS 1030 and 1200), after which an
322   updated offset point p was used to replace the 0.2 % offset point. Subsequently, the conventional R-O
323   relations were updated shown in Eq. (19)

324
$$\varepsilon = \begin{cases} \dfrac{\sigma}{E_s} + p\left(\dfrac{\sigma}{f_p}\right)^{n} & \text{for } 0 \leq \sigma \leq f_p \\[4mm] \dfrac{\sigma - f_p}{E_p} + \left(\varepsilon_{eu} - \varepsilon_p - \dfrac{f_{eu} - f_p}{E_p}\right)\left(\dfrac{\sigma - f_p}{f_{eu} - f_p}\right)^{m} + \varepsilon_p & \text{for } f_p < \sigma \leq f_{eu} \end{cases}$$
(19)

325   where E_p is the tangent modulus at offset point of f_p, ε_{eu} which can be determined by Eq. (20) and f_{eu} are the
326   strain and the corresponded stress at the equivalent ultimate point.

327
$$E_p = \left.\frac{\partial \varepsilon(\sigma)}{\partial \sigma}\right|_{\sigma=f_p} = \left.\frac{1 + pn\dfrac{\sigma}{f_p}^{n}E}{E}\right|_{\sigma=f_p} = \frac{1 + pn\dfrac{E}{f_p}}{E}$$
(20)

328   The schematic view of the stress-strain curve with re-assigned offset point can be seen in Fig. 15.
329   Conventional 0.2% plastic strain is being replaced by a new point p between the first stage (stage i) and the
330   second stage (stage ii). The second stage (stage ii) starts from the re-defined offset point and ends at an
331   equivalent ultimate point, which was defined to be 99% of the ultimate strength. A straight line is used to
332   connect the equivalent ultimate point and the ultimate strength for simplicity (stage iii). The proposed offset

9

333 point was proportional to the ratio of ultimate strength to yield strength. The relationship between the offset
334 point p and the ratio of ultimate strength to yield strength is provided for HSS. It should be noted that Fang
335 et al. [29] conducted material properties and residual stresses investigation for HSS OctHS with nominal
336 yield strength of 690 MPa, the stress-strain model for HSS OctHS was also proposed as follows in Eqs. (21)
337 – (23).

338

339 $$\varepsilon = \begin{cases} \dfrac{\sigma}{E} + 0.002(\dfrac{\sigma}{f_{0.2}})^n & \text{for} \quad \sigma \le f_{0.2} \\[2em] \dfrac{\sigma - f_{0.2}}{E_{0.2}} + (\varepsilon_u - \varepsilon_{0.2} - \dfrac{f_u - f_{0.2}}{E_{0.2}})(\dfrac{\sigma - f_{0.2}}{f_u - f_{0.2}})^m + \varepsilon_{0.2} & \text{for} \quad f_{0.2} \ge \sigma \end{cases} \tag{21}$$

340 where n and m are derived as follows,

341 $$n = \begin{cases} \dfrac{\ln(0.2/0.01)}{\ln(f_{0.2}/f_{0.01})} + \log_{\frac{f_u}{f_{0.2}}} (\varepsilon_u/0.002) & \text{for flat portion} \\[2em] \dfrac{\ln(0.2/0.01)}{\ln(f_{0.2}/f_{0.01})} & \text{for corner portion} \end{cases} \tag{22}$$

342 $$m = \dfrac{\ln(\varepsilon_u/\varepsilon_{0.2})}{\ln(f_u/f_{0.2})} \tag{23}$$

343

3.5.1.2. Proposed stress-strain models for HSS IOctHS with rounded responses

345

346 The existing stress-strain models introduced in the previous section for non-linear metallic materials with
347 rounded response are compared and assessed using the experimental results generated in this study for flat
348 and corner coupon specimens. The multi-stage model from Hradil [41], the offset point model from Xia et
349 al. [42], generic stress-strain model for cold-formed carbon steel from Gardner and Yun [38] as well as the
350 model proposed in Fang et al. [29] for HSS OctHS were evaluated based on the experiment results for HSS
351 IOctHS.

352

353 The comparisons between the experimental curves and the predictions from the stress-strain models for flat
354 coupon specimens of IOctHS145×6-1.50-F4, and IOctHS225×6-2.00-F6 are plotted in Fig. 16. As depicted
355 in Fig. 16(a), the first stage of the experimental data from the specimen IOctHS145×6-1.50-F4 correlated
356 well with the predicted model from Gardner and Yun [38] and Hradil et al. [41], whereas the model from
357 Fang et al. [29] slightly over-estimate the strain. In terms of the second stage after reaching the yield point
358 as shown in Fig. 16(b), the experimental curve played as lower bound with underestimated strain from
359 predicted models, indicating the deficiency of the existing stress-strain models. In prediction of the first stage
360 for flat coupon specimens of IOctHS225×6-2.00-F6, as shown in Fig. 16 (c), the models from Gardner and
361 Yun [38] and Hradil et al. [41] accurately capture the stress-strain path in the first stage of the stress-strain
362 curve whereas the model from Fang et al. [29] slightly over-estimates the development of strain. The
363 predictions based on Xia et al. [42] model largely deviated from the experimental data. Predictions derived
364 from these stress-strain models all generate the under-estimated strain at the beginning of the second stage
365 and become over-conservative in predicting the stress near the ultimate strength, as shown in Fig 16(d).
366 Upon on the comparisons between the test results and the predicted models, the stress-strain models from

367 Gardner and Yun [38] and Hradil et al. [41] give comparable results. For the flat coupon specimens in the
368 first stage. Note however that regression analysis is required to derive the exponential component n in Hradil
369 et al. [41] model which limit its application in practice. Therefore, the stress-strain model from Gardner and
370 Yun [38] is suggested being used to predict the stress-strain relationship for HSS IOctHS in first stage up to
371 the 0.2% proof strength due its simplicity.

373 Figs. 17 (a)–(d) display the comparisons between the experimental curves of corner coupon specimens
374 extracted from sections of IOctHS145×6-1.50-C6 and IOctHS225×6-2.00-C7. In terms of the comparison
375 results for corner coupon specimens, the predictions obtained from the model provided by Gardner and Yun
376 [38] successfully replicate the stress-strain path for first stage stress-strain curves of corner coupon specimen
377 of IOctHS145×6-1.50-C6, whereas Xia et al. [42] model largely under-estimates the strain near yield
378 strength, as shown in Fig. 17(a). The model from Fang et al. [29] provides over-estimated strain in the first
379 stage. As seen in Fig. 17 (b), the stress-strain models from Gardner and Yun [38] and Fang et al. [29] give
380 comparable results for the stress-strain relations in second stage after yield point. Likewise, for corner
381 coupon specimen of IOctHS225×6-2.00-C7, Xia et al. [42] model gives under-estimated results whereas
382 Fang et al. [29] over-predict the strain development for first stage. The model provided in Gardner and Yun
383 [38] generate good agreement between the test results and the predictions. It should be noted that the stress-
384 strain model from Fang et al. [29] achieve more accurate predictions for the stress-strain curves in second
385 stages than the one proposed by Gardner and Yun [38], as shown in Fig. 17(b) and Fig. 17(d).

387 Based on the comparison between the numerous models for flat and corner coupon specimens, the stress-
388 strain model from Gardner and Yun [38] can be used for constructing stress-strain relationship for first stage
389 of flat and corner coupon specimens. The model proposed in Fang et al. [29] can be used for predicting the
390 second stage stress-strain curves for corner coupon specimens.

392 A new model which can accurately predict the second stage stress-stain response needs to be developed for
393 flat coupon specimens. Based on the aforementioned discussions and the characteristics of the stress-strain
394 curves of flat coupon specimens, only minimal increase is observed after the first turning point (yield point),
395 as shown in Figs. 16(a) and 16(c). It may cause the over-estimation for second stage in terms of the strain
396 than the experimental curve simply using the conventional 0.2% proof strength or re-defined 1.0% proof
397 strength, as shown in Figs. 16(b) and 16(d). In light of the non-linear regression analysis, an offset point
398 with plastic strain of 0.1% is proposed for second stage estimation. The elastic modulus corresponding to
399 0.5% plastic strain was suggested due to the lower level of strain hardening after the turning point, which is
400 provided as follows, in Eq. (24)

402
$$E_{0.5} = \left.\frac{\partial \sigma}{\partial \varepsilon}\right|_{\varepsilon=\varepsilon_{0.5}} = \frac{E}{1 + \varepsilon_{0.5} n (\frac{\sigma}{f_{0.5}})^{n-1} \frac{E}{f_{0.5}}}$$
(24)

403 To build the stress-strain curve for flat coupon specimens in second stage, additional parameters are needed
404 including $f_{0.1}, f_u, \varepsilon_u$, and exponential coefficient m. In practice, yield strength $f_{0.2}$ is provided. If relationships
405 between the additional parameters and the yield strength $f_{0.2}$ can be found, it will largely simplify the use of
406 the proposed model. To develop the relationships between these parameters, yield strength $f_{0.2}, f_{0.1}, f_u, \varepsilon_u$, and
407 m from the test results in this study and Fang et al. [29] were used. The relationship between the required

408   parameter $f_{0.1}$ and yield strength $f_{0.2}$ is plotted in Fig. 18. In addition to the linear fit expression, two trend-
409   lines with ±1% variance were used. All data points locate in the ±1% variance trend-lines demonstrating the
410   accuracy of the linear fit expression. Thus, the relation between the $f_{0.1}$ and yield strength can be expressed
411   using Eq. (25).

413   $$f_{0.2} = 1.025 f_{0.1} + 13.15 \tag{25}$$

415   A linear relationship between the ultimate strength f_u and the 0.1% proof strength $f_{0.1}$ was found and the
416   experimentally obtained f_u is plotted against the 0.1% proof strength in Fig. 19 with two trend-lines of ±1%
417   variance. Most of the test data locate between the two trend-lines illustrating the accuracy of the linear fit
418   relationships and the expression is obtained as Eq. (26).

420   $$f_u = 1.275 f_{0.1} + 160 \tag{26}$$

422   Ultimate strain ε_u is also one of the parameters required for constructing the stress-strain curves. However,
423   the steel manufacturer may not always provide it. Hence, Liu et al. [33] collated the existing database for
424   HSS with nominal yield strength of 690 MPa and proposed an expression between the ultimate strain and
425   the normalized strength ratio of yield strength over ultimate strength. Expressions between these parameters
426   were also proposed by Gardner and Yun [38] which relate the ultimate strain to normalized ratio of yield
427   strength to ultimate strength for cold-formed steels. These two proposed expressions are plotted in Fig. 20
428   in comparison to the experimental data. As can be seen in the Fig. 20, the equation proposed by Gardner and
429   Yun locate below the experimental data as the lower bound and the model proposed in Liu et al. [33]
430   correlates well with the experimental data. Hence, the expression from Liu et al. [33] is employed for
431   building the second stage stress-strain curve.

433   As introduced in the previous section, the exponential parameter m determines the extent of the non-linearity
434   of the stress-strain curve in second stage. Based on the regression analysis, there is a linear relationship
435   between the exponential parameter m and the normalized stress ratio between the yield strength and the
436   ultimate strength. In Fig. 21, a linear regression line incorporating with two trend-lines with ±10% variance
437   are added to the graph. The expression of the linear relation is derived in Eq. (27).

439   $$m = 345.2 \frac{f_{0.2}}{f_u} - 285.9 \tag{27}$$

440   **3.5.2. Stress-strain model for coupon specimens with yield plateau**

442   Different from the material model for the stress-strain relationship with rounded response, a suitable stress-
443   strain model to describe the stress-strain relationship with yield plateau is also required. Quad-linear material
444   model was proposed by Boeraeve et al. [43] and further revised by Yun and Gardner [44] for hot-rolled steel
445   materials with strain hardening after yield plateau. To trace the gradual loss of the stiffness, a power model
446   was proposed, as shown in Eq. (28).

447
$$\sigma \begin{cases} E_s \varepsilon & \text{for } \varepsilon \le \varepsilon_y \\ f_y & \text{for } \varepsilon_y \le \varepsilon \le \varepsilon_{sh} \\ f_y + (f_u - f_y)[0.4\varepsilon_x + 2\varepsilon_x / (1 + 400\varepsilon_x^5)^{\frac{1}{5}}] & \text{for } \varepsilon_{sh} \le \varepsilon \le \varepsilon_u \end{cases} \tag{28}$$

448 where ε_x is equal to $(\varepsilon\text{-}\varepsilon_{sh})/(\varepsilon_u\text{-}\varepsilon_{sh})$.

449

450 It should be noted that hardening strain ε_{sh} is generally not provided in the mill certificates and it is obtained

451 based on the non-linear regression analysis as follows, from Eqs. (29) – (30).

452

453
$$\varepsilon_{sh} = 0.1\frac{f_y}{f_u} - 0.055 \qquad \text{for } 0.015 \le \varepsilon_{sh} \le 0.03 \tag{29}$$

454
$$\varepsilon_u = 0.6(1 - \frac{f_y}{f_u}) \qquad \text{for } \varepsilon_{sh} \ge 0.06 \tag{30}$$

455 Note that non-linear strain hardening markedly resembles the initial part of Ramberg-Osgood model up to

456 0.2% proof strength. A modified Ramberg-Osgood model to describe the stress-strain behaviour of the non-

457 linear strain-hardening range was proposed for Q690 steel with certain level of non-linear strain hardening

458 [33]. The strain hardening range starts at the point where the yield plateau ends as the origin of stain

459 hardening curve depicted in Figs. 22–23. The stress-strain relationship can be expressed by Eq. (32)

460

461
$$\varepsilon - \varepsilon_{sh} = \frac{\sigma - f_y}{E_{sh}} + \left(\varepsilon_u - \varepsilon_{sh} - \frac{f_u - f_y}{E_{sh}}\right)\left(\frac{\sigma - f_y}{f_u - f_y}\right)^m \tag{31}$$

462

463
$$\begin{aligned} &(1)\ \text{Bilinear: } \sigma = \begin{cases} E_s\varepsilon & \text{for } \varepsilon \le \varepsilon_y \\ f_y & \text{for } \varepsilon_y < \varepsilon \le \varepsilon_{sh} \end{cases} \\ &(2)\ \text{nonlinear: } \varepsilon = \varepsilon_{sh} + \frac{\sigma - f_y}{E_{sh}} + \left(\varepsilon_u - \varepsilon_{sh} - \frac{f_u - f_y}{E_{sh}}\right)\left(\frac{\sigma - f_y}{f_u - f_y}\right)^m \text{ for } \sigma > f_y \end{aligned} \tag{32}$$

464 where E_{sh} is the initial slope of the stress-strain curves in the strain-hardening range, also termed as hardening

465 modulus. E_{sh} can be directly obtained from material tests. If the value is not reported, Eq. (33) proposed in

466 Yun and Gardner [44] might be used to calculate its value.

467

468
$$E_{sh} = \frac{f_u - f_y}{0.4(\varepsilon_u - \varepsilon_{sh})} \tag{33}$$

469 ε_u and ε_{sh} are proposed based on the experimental results in this study and test results from Q690 steel in

470 [33].

471
$$\varepsilon_{sh} = 0.2\frac{f_y}{f_u} + 0.2 \qquad \text{for } 0.015 \le \varepsilon_{sh} \le 0.03 \tag{34}$$

472 $$\varepsilon_{\text{u}} = 0.8(1 - \frac{f_y}{f_u}) \qquad \text{for } \varepsilon_{\text{sh}} \geq 0.06 \tag{35}$$

473 In Fig. 22, comparisons of stress-strain curves between experimental results with yield plateau and that
474 obtained based on the predictive model for the flat coupon specimen of IOctHS145×6-1.50-F2 are presented.
475 The strain was over-predicted by Yun and Gardner's [44] model at the same stress level, whereas the
476 proposed method can trace the gradual decreasing stiffness of the stress-strain path in hardening stage
477 accurately. Similarly, the derived stress-strain path from Yun and Gardner's [44] model slightly deviated
478 from the test data with over-predicted stress in the mid-stage of strain hardening for the specimen
479 IOctHS145×10-1.50-F7, as shown in Fig. 23. The black dashed line in Fig. 23(b) is the predicted data based
480 on the proposed model which precisely follow the stress-strain path in the strain hardening range.

481

482 **4. Residual stresses investigation**

483

484 Residual stresses existing in the cold-formed steel structures can adversely affect the structural performance
485 due to premature yielding and reducing the structural resistance. Residual stresses in the structural element
486 are primarily generated during the manufacturing processes such as cold-forming process associated press-
487 braking and cold-rolling. Aside from the cold-forming processes, welding also induces residual stress as a
488 result of the uneven cooling and heating [45]. The residual stresses in steel structures can be considered in
489 both longitudinal and transverse directions. Ziemian [46] and Schafer et al. [47] demonstrate that the residual
490 stresses in the longitudinal direction have the most significant effect on the structures, therefore, longitudinal
491 residual stresses were investigated in this study. Moreover, residual stresses can be further decomposed into
492 membrane and bending residual stresses based on the distribution through the thickness of the hollow section
493 [48].

494

495 **4.1. Measurement of the residual stresses**

496

497 Up to now, numerous measuring techniques were capable of providing accurate results for the magnitude
498 and distribution of the residual stresses, which can be classified as destructive method and non-destructive
499 method. X-ray diffraction method, neutron or electron diffraction method, ultrasonic method and magnetic
500 methods are classified as non-destructive methods while destructive methods mainly comprise of sectioning
501 method and hole drilling method. Numerous investigations for residual stress magnitude and distribution
502 have been successfully employed for cold-formed sections and built-up sections using the sectioning method
503 and hole drilling method, as presented in Table. 9. In this investigation, the sectioning method by wire cutting
504 was used to measure the magnitudes of the residual stresses for cold-formed HSS IOctHS. The effect of
505 membrane and bending residual stresses on deformation of the strips after cutting are illustrated in Fig. 24.

506

507 The specimens of IOctHS145×6-1.50, IOctHS220×6-1.50, IOctHS225×6-2.00 and IOctHS145×10-1.50
508 sections were investigated. The length of the specimen is 400 mm. Quarter sections of the cold-formed HSS
509 IOctHS were marked longitudinally with strip width varying between 10 mm and 12 mm depending on the
510 stress gradient prior to sectioning. Strain gauges of model FLAB-5-11-1LJC-F made by Tokyo Sokki
511 Kenkyujo with a 5 mm gauge length were employed with the capacity of measuring strains up to 5%. The
512 strain gauges were affixed to the outer and inner surfaces at mid-height of the marked longitudinal strips as
513 shown in Fig. 25. A waterproof tape was used to protect the strain gauges to avoid damage. The initial

514 readings from the strain gauges were recorded prior to the cutting process. To minimize the heat generated
515 during the process of wire-cutting, coolant was used, as shown in Fig. 26. After the wire-cutting process, the
516 residual stresses were released from the strips. The readings from the strain gauges were extracted again. It
517 should be noted that readings for at least three times were recorded and the mean value was derived as the
518 representative magnitude. There were 55 strips cut by wire-cutting and more than 660 strain data were
519 recorded. The difference between the initial and final readings represents the strain released during the
520 cutting of each strip. The magnitude of the bending and membrane residual stresses can be determined based
521 on the relationships as follows, in Eq. (36) and Eq. (37).

$$\sigma_{\mathrm{m}} = -\,(\frac{\Delta\varepsilon_{\mathrm{ext}} + \Delta\varepsilon_{\mathrm{int}}}{2})E_{\mathrm{s}} \tag{36}$$

$$\sigma_{\mathrm{b}} = -\,(\frac{\Delta\varepsilon_{\mathrm{ext}} - \Delta\varepsilon_{\mathrm{int}}}{2})E_{\mathrm{s}} \tag{37}$$

524 where $\Delta\varepsilon_{\mathrm{ext}}$ is the difference between the initial strain readings and the final srain readings after wire-cutting
525 for external strain gauge, $\Delta\varepsilon_{\mathrm{int}}$ is the the difference between the initial strain readings and the final srain
526 readings after wire-cutting for internal strain gauge.
527
528 **4.2. Results and discussions**
529
530 The elastic deformation of the longitudinal marked strips was released after completion of the wire-cutting
531 process. The strips extracted in the vicinity of the cold-bent corner regions significantly curved due to
532 relatively large bending residual stresses. The strips taken from the cold formed HSS IOctHS specimens are
533 presented in Fig. 27. The membrane and bending residual stresses were determined by Eqs. (36) – (37) with
534 positive and negative values indicating the tensile and compressive residual stresses respectively. The
535 obtained magnitudes of the residual stresses were normalized to the average yield strength of the parent steel
536 plate and plotted against the distance from the welding seam.
537
538 As can be seen in Fig. 28, the largest membrane residual stresses for IOctHS145×6-1.50 occurred at the
539 location near the welding seam reaching about 52.8% of the yield strength of the parent plate. The tensile
540 membrane residual stresses gradually decreased and changed to compressive residual stresses at first cold-
541 bent corner (between the long flat portion and short flat portion). The membrane residual stresses changed
542 to tensile stresses when approaching to the second cold-bent corner (between the two short flat portions).
543 The largest bending residual stresses were found to be much larger at the corner region in comparison with
544 those in the flat portion for IOctHS145×6-1.50. The maximum tensile bending residual stresses was 36.7%
545 of the $f_{0.2,\mathrm{p}}$ of the parent plate at the second cold-bent corner whereas the bending residual stresses at the first
546 corner was 29.7% of the $f_{0.2,\mathrm{p}}$ of the parent plate.
547
548 Fig. 29 displays the membrane and bending residual stresses distribution of the HSS IOctHS220×6-1.50.
549 The bending residual stresses are 18% and 35% of the $f_{0.2,\mathrm{p}}$ of the parent plate for the at the first and the
550 second corners respectively. The largest membrane residual stresses were 62.9% at the welding seam. For
551 membrane residual stresses of specimen IOctHS225×6-2.00, the largest membrane residual stresses reached
552 59.4% of the $f_{0.2,\mathrm{p}}$ of the parent plate, and the largest bending residual stresses was 54.2% at second corner,
553 which was larger than the bending residual stresses at first cold-bent corner indicating the severe plastic

deformation during the process of press-braking, shown in Fig. 30. For residual stresses distribution of specimen IOctHS145×10-1.50, the membrane residual stresses was the largest among all the sections with a magnitude of 66.5% of the $f_{0.2,p}$ and the largest bending residual stresses reached at 36.1% of the $f_{0.2,p}$ of the parent plate at the second corner, as depicted in Fig. 31. Based on the comparisons between the distribution patterns of HSS IOctHS in terms of both membrane and bending residual stresses, consistent residual stress patterns were found for the investigated sections, demonstrating the negligible effect of the dimensions on the residual stresses distribution.

4.3. Proposed model for residual stresses distribution

To allow for accurate predictions of structural behaviour of HSS IOctHS members, a predictive model for residual stresses distribution was developed based on the test results of the residual stresses measurements. For the ease of the application, a multi-linear model was adopted as the simplified distribution of residual stresses with constant values at corners for bending residual stresses. It has been successfully adopted in predictive models for conventional strength steel OctHS with nominal yield strength of 355 MPa [13] and HSS OctHS with nominal yield strength of 460 MPa [19] and 690 MPa [29], as shown in Fig. 32. The magnitudes of the residual stresses in the predictive model were derived as the average membrane and bending residual stresses over different locations of the hollow sections. The total net forces of the outer stresses and the inner stresses are zero. In Fig. 33, the predicted residual stresses distribution based on the proposed model was plotted against the distance from the welding seam in a normalized form against the average yield strength of the parent plate $f_{0.2,p}$.

5. Conclusions

The material properties variations and the residual stresses distributions in cold-formed HSS IOctHS with varying aspect ratios have been experimentally investigated in this study. To investigate the material properties variations, tensile coupon specimens were extracted from critical locations within the cross sections of the cold-formed HSS IOctHS. Strength enhancement can be observed from the tensile coupon specimens taken from the corner portions underlining the cold-formed effect of the press-braking on the material properties. In addition to the tensile coupon tests, obtained material properties were compared and assessed against the codified requirements on material properties in EN 1993-1-12. The results show that all the flat coupon specimens meet the requirement specified in EN 1993-1-12, whereas corner coupon specimens cannot meet the requirement on ductility due to the large plastic deformation experienced during press-braking fabrication. Enhancement of 5.2% in yield strength can be observed from specimen of IOctHS225×6-2.00 and an increment of 8.4% for corner coupon specimen from IOctHS145×10-1.50 was obtained.

The applicability of the existing material models to the stress-strain relationship for the coupon specimens taken from both flat portions and corner portions was compared and evaluated against the experimental results. It was found that the predictive model proposed by Gardner and Yun can be adopted to predict the stress-strain relationships for the flat and corner coupon specimens in the first stage up to 0.2% proof strength and the model proposed by Han et al. can provide accurate predictions for the corner coupon specimens taken from IOctHS in the second stage after the yield point. Moreover, new material models to construct the stress-strain responses for flat coupon specimens with rounded response or yield plateau are developed and

598   proposed.

599

600   Experimental investigation on residual stress magnitude and distribution pattern of HSS cold-formed IOctHS

601   was also reported and discussed. Membrane and bending residual stresses in cold-formed HSS IOctHS were

602   measured through the sectioning method. The distributions of the membrane and bending residual stresses

603   are presented. Among all the HSS IOctHS, the largest membrane residual stresses with a magnitude of 66.5%

604   of the $f_{0.2,p}$ was found from IOctHS145×10-1.50, whereas the largest bending residual stresses reach at 54.2%

605   of $f_{0.2,p}$ from the IOctHS225×6-2.00. It was also observed that the residual stress distribution is insensitive

606   to the dimensions of IOctHS. Furthermore, a predictive model for residual stresses distribution and

607   magnitudes was proposed. The proposed residual stress distribution model can be applied in the structural

608   analysis and design for HSS IOctHS with aspect ratio varying from 1.0 to 2.0.

609

610   **Acknowledgements**

611

619

620   References

621   [1] J.-L. Ma, T.-M. Chan, B. Young, Material properties and residual stresses of cold-formed high strength

622   steel hollow sections, J. Constr. Steel. Res. 109 (2015) 152-165.

623   [2] J. Chen, H. Fang, T.-M. Chan, Design of fixed-ended octagonal shaped steel hollow sections in

624   compression, Eng. Struc. 228 (2021) 111520.

625   [3] L. Gao, H. Sun, F. Jin, H. Fan, Load-carrying capacity of high-strength steel box-sections I: Stub columns,

626   J. Constr. Steel. Res. 65 (2009) 918-924.

627   [4] G. Shi, J. Wang, Y. Bai, Y. Shi, Experimental study on seismic behavior of 460MPa high strength steel

628   box-section columns, Adv Struct Eng. 17 (2014) 1045-1059.

629   [5] J.L. Ma, T.M. Chan, B. Young, Experimental Investigation on Stub-Column Behavior of Cold-Formed

630   High-Strength Steel Tubular Sections, J. Struct. Eng. 142 (2016) 04015174.

631   [6] B. Somodi, B. Kövesdi, Flexural buckling resistance of cold-formed HSS hollow section members, J.

632   Constr. Steel. Res. 128 (2017) 179-192.

633   [7] H. Fang, T.-M. Chan, B. Young, Structural performance of cold-formed high strength steel tubular

634   columns, Eng. Struc. 177 (2018) 473-488.

635   [8] H. Fang, T.-M. Chan, Resistance of Axially Loaded Hot-finished S460 and S690 Steel Square Hollow

636   Stub Columns at Elevated Temperatures, Structures. 17 (2019) 66-73.

637   [9] X. Meng, L. Gardner, Behavior and Design of Normal-and High-Strength Steel SHS and RHS Columns,

638   J. Struct. Eng. 146 (2020) 04020227.

639   [10] X. Meng, L. Gardner, Cross-sectional behaviour of cold-formed high strength steel circular hollow

640   sections, Thin-Walled Struct. 156 (2020) 106822.

641   [11] B. Evirgen, A. Tuncan, K. Taskin, Structural behavior of concrete filled steel tubular sections (CFT/CFSt)

642   under axial compression, Thin-Walled Struct. 80 (2014) 46-56.

643   [12] A.T. Tran, M. Veljkovic, C. Rebelo, L.S. da Silva, Resistance of cold-formed high strength steel circular

644   and polygonal sections — Part 1: Experimental investigations, J. Constr. Steel. Res. 120 (2016) 245-257.

645   [13] J.Y. Zhu, T.M. Chan, B. Young, Cross-sectional capacity of octagonal tubular steel stub columns under

646   uniaxial compression, Eng. Struc. 184 (2019) 480-494.

647   [14] J.S. Kabanda, MacDougall, Comparison of the moment rotation capacities of rectangular and polygonal

648   hollow sections, J. Constr. Steel. Res. 137 (2017) 66-76.

649   [15] P.S. Bulson, The strength of the thin-walled tubes formed from flat elements, Int. J. Mech. Sci. 11 (1969)

650   613-620.

651   [16] W. Naohiro, I. Kikuo, O. Tadayoshi, K. Yosuke, 05.11: Local buckling behavior of octagonal hollow

652   cross-section member under axial compression or bending shear, ce/papers. 1 (2017) 1116-1122.

653   [17] H. Fang, T.-M. Chan, B. Young, Structural performance of concrete-filled cold-formed high-strength

654   steel octagonal tubular stub columns, Eng. Struc. 239 (2021) 112360.

655   [18] H. Fang, T.-M. Chan, B. Young, Experimental and Numerical Investigations of Octagonal High-

656   Strength Steel Tubular Stub Columns under Combined Compression and Bending, J. Struct. Eng. 147 (2021)

657   04020282.

658   [19] J. Chen, H. Liu, T.-M. Chan, Material properties and residual stresses of cold-formed octagonal hollow

659   sections, J. Constr. Steel. Res. 170 (2020) 106078.

660   [20] J.Y. Zhu, T.M. Chan, Experimental investigation on octagonal concrete filled steel stub columns under

661   uniaxial compression, J. Constr. Steel. Res. 147 (2018) 457-467.

662   [21] P. Manoleas, E. Koltsakis, M. Veljkovic, 03.16: Multiplanar K-joints on cold-formed open sections: An

663   experimental study with high strength steels, ce/papers. 1 (2017) 629-638.

664   [22] J. Chen, J.-Y. Zhu, T.-M. Chan, Experimental and numerical investigation on stub column behaviour of

665   cold-formed octagonal hollow sections, Eng. Struc. 214 (2020) 110669.

666   [23] H. Fang, T.-M. Chan, B. Young, Behavior of Octagonal High-Strength Steel Tubular Stub Columns, J.

667   Struct. Eng. 145 (2019) 04019150.

668   [24] T. Reinke, P. Knoedel, T. Ummenhofer, Steel poles with polygonal sections in bending, European

669   Conference on Steel and Composite Structures, Naples, Italy, 2014,

670   [25] Z.M. Dalia, A.K. Bhowmick, G.Y. Grondin, Local buckling of multi-sided steel tube sections under

671   axial compression and bending, J. Constr. Steel. Res. 186 (2021) 106909.

672   [26] K. Sefcikova, T. Brtnik, J. Dolejs, K. Keltamaki, R. Topilla, Mechanical properties of heat affected zone

673   of high strength steels, IOP Conference Series: Materials Science and Engineering, 96, 2015, 012053

674   [27] X. Liu, K.-F. Chung, H.-C. Ho, M. Xiao, Z.-X. Hou, D.A. Nethercot, Mechanical behavior of high

675   strength S690-QT steel welded sections with various heat input energy, Eng. Struc. 175 (2018) 245-256.

676   [28] B. Somodi, B. Kovesdi, Residual stress measurements on welded square box sections using steel grades

677   of S235-S960, Thin-Walled Struct. 123 (2018) 142-154.

678   [29] H. Fang, T.-M. Chan, B. Young, Material properties and residual stresses of octagonal high strength

679   steel hollow sections, J. Constr. Steel. Res. 148 (2018) 479-490.

680   [30] ISO 17636-2, Non-destructive testing of welds — Radiographic testing — Part 2: X- and gamma-ray

681   techniques with digital detectors, International Organization for Standardization, 2013.

682   [31] EN ISO 6892-1, Metallic Materials – Tensile Testing Part 1: Method of Test at Ambient Temperature,

683   CEN, Brussels, Belgium, 2019.

684   [32] Y. Huang, B. Young, The art of coupon tests, J. Constr. Steel. Res. 96 (2014) 159-175.

685   [33] Liu J-Z, Fang H, Chen S, Chan T-M. Material properties and residual stresses of high strength steel

686 hexagonal hollow sections. J Constr Steel Res. 190 (2022) 107061.

687 [34] EN 1993-1-12, Eurocode 3: Design of Steel Structures – Part 1–12: Additional Rules for the Extension
688 of EN 1993 up to Steel Grades S700, European Committee for Standardization (CEN), Brussels, 2007.

689 [35] H. Hill, Determination of stress-strain relations from" offset" yield strength values, Aluminum Co Of
690 America Pittsbrugh Pa, 1944.

691 [36] E. Mirambell, E. Real, On the calculation of deflections in structural stainless steel beams: an
692 experimental and numerical investigation, J. Constr. Steel. Res. 54 (2000) 109-133.

693 [37] K.J. Rasmussen, Full-range stress–strain curves for stainless steel alloys, J. Constr. Steel. Res. 59 (2003)
694 47-61.

695 [38] L. Gardner, X. Yun, Description of stress-strain curves for cold-formed steels, Constr. Build. Mater. 189
696 (2018) 527-538.

697 [39] I. Arrayago, E. Real, L. Gardner, Description of stress–strain curves for stainless steel alloys, Mater.
698 Des. 87 (2015) 540-552.

699 [40] K. Abdella, Inversion of a full-range stress–strain relation for stainless steel alloys, International Journal
700 of Non-Linear Mechanics. 41 (2006) 456-463.

701 [41] P. Hradil, A. Talja, E. Real, E. Mirambell, B. Rossi, Generalized multistage mechanical model for
702 nonlinear metallic materials, Thin-Walled Struct. 63 (2013) 63-69.

703 [42] Y. Xia, C. Ding, Z. Li, B.W. Schafer, H.B. Blum, Numerical modeling of stress-strain relationships for
704 advanced high strength steels, J. Constr. Steel. Res. 182 (2021) 106687.

705 [43] P. Boeraeve, B. Lognard, J. Janss, J. Gerardy, J. Schleich, Elasto-plastic behaviour of steel frame works,
706 J. Constr. Steel. Res. 27 (1993) 3-21.

707 [44] X. Yun, L. Gardner, Stress-strain curves for hot-rolled steels, J. Constr. Steel. Res. 133 (2017) 36-46.

708 [45] Y.-F. Hu, K.-F. Chung, H. Ban, D.A. Nethercot, Investigations into residual stresses in S690 cold-formed
709 circular hollow sections due to transverse bending and longitudinal welding, Eng. Struc. 219 (2020) 110911.

710 [46] R.D. Ziemian, Guide to stability design criteria for metal structures, John Wiley & Sons, 2010.

711 [47] B.W. Schafer, Z. Li, C.D. Moen, Computational modeling of cold-formed steel, Thin-Walled Struct. 48
712 (2010) 752-762.

713 [48] R. Cruise, L. Gardner, Residual stress analysis of structural stainless steel sections, J. Constr. Steel. Res.
714 64 (2008) 352-366.

715 [49] EN 10025-6, Hot rolled products of structural steels – Part 6: Technical delivery conditions for flat
716 products of high yield strength structural steels in the quenched and tempered condition, European
717 Committee for Standardization (CEN), Brussels, 2004.

718 [50] C.K. Lee, S.P. Chiew, J. Jiang, Residual stress study of welded high strength steel thin-walled plate-to-
719 plate joints, Part 1: Experimental study, Thin-Walled Struct. 56 (2012) 103-112.

720 [51] Y.-B. Wang, G.-Q. Li, S.-W. Chen, The assessment of residual stresses in welded high strength steel
721 box sections, J. Constr. Steel. Res. 76 (2012) 93-99.

722 [52] H. Ban, G. Shi, Y. Bai, Y. Shi, Y. Wang, Residual stress of 460 MPa high strength steel welded I section:
723 experimental investigation and modeling, Int. J. Steel Struct. 13 (2013) 691-705.

724 [53] H. Ban, G. Shi, Y. Shi, Y. Wang, Residual stress of 460 MPa high strength steel welded box section:
725 Experimental investigation and modeling, Thin-Walled Struct. 64 (2013) 73-82.

726 [54] C.K. Lee, S.P. Chiew, J. Jiang, Residual stress of high strength steel box T-joints: Part 1: Experimental
727 study, J. Constr. Steel. Res. 93 (2014) 20-31.

728 [55] T.-J. Li, G.-Q. Li, Y.-B. Wang, Residual stress tests of welded Q690 high-strength steel box-and H-
729 sections, J. Constr. Steel. Res. 115 (2015) 283-289.

730   [56] M. Khan, A. Paradowska, B. Uy, F. Mashiri, Z. Tao, Residual stresses in high strength steel welded box
731   sections, J. Constr. Steel. Res. 116 (2016) 55-64.

732   [57] C. Yang, J. Yang, M. Su, Y. Li, Residual stress in high-strength-steel welded circular tube, Proc. Inst.
733   Civil Eng.-Struct. Build. 170 (2017) 631-640.

734   [58] X. Liu, K.-F. Chung, Experimental and numerical investigation into temperature histories and residual
735   stress distributions of high strength steel S690 welded H-sections, Eng. Struc. 165 (2018) 396-411.

736   [59] Y. Sun, Y. Liang, O. Zhao, Testing, numerical modelling and design of S690 high strength steel welded
737   I-section stub columns, J. Constr. Steel. Res. 159 (2019) 521-533.

738   [60] J. Chen, T.-M. Chan, Material properties and residual stresses of cold-formed high-strength-steel
739   circular hollow sections, J. Constr. Steel. Res. 170 (2020) 106099.

740   [61] J. Chen, W.-l. Jin, Corner strength enhancement of high strength cold-formed steel at normal room and
741   elevated temperatures, Journal of Zhejiang University-SCIENCE A. 9 (2008) 1251-1257.

742   [62] A. Su, Y. Sun, Y. Liang, O. Zhao, Material properties and membrane residual stresses of S690 high
743   strength steel welded I-sections after exposure to elevated temperatures, Thin-Walled Struct. 152 (2020)
744   106723.

745   [63] A. Su, Y. Sun, Y. Liang, O. Zhao, Membrane residual stresses and local buckling of S960 ultra-high
746   strength steel welded I-section stub columns, Thin-Walled Struct. 161 (2021) 107497.

747   [64] L. Moen, O. Hopperstad, M. Langseth, Rotational capacity of aluminium beams subjected to non-
748   uniform bending—Part I: Experiments, Journal of Structural Engineering ASCE. 125 (1999) 910-920.

Fig. 1. Application of the octagonal sections in civil engineering structures (a) Octagonal section lighting column (Zhuhai, China) (b) Octagonal section steel columns (Shenzhen, China).
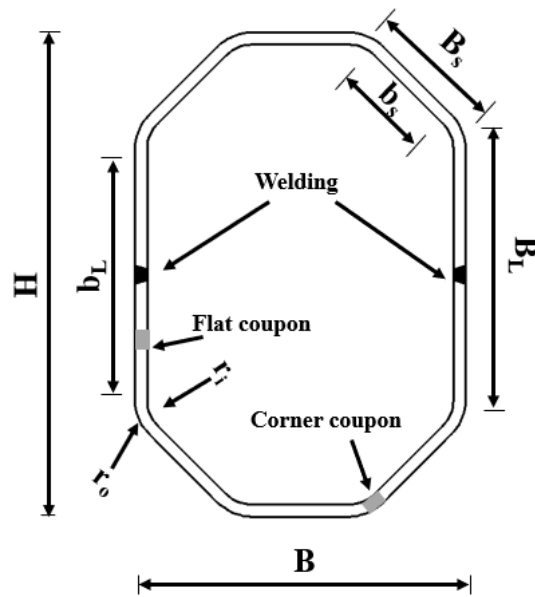
Fig. 2. Cross section of the HSS cold-formed irregular octagonal hollow sections.
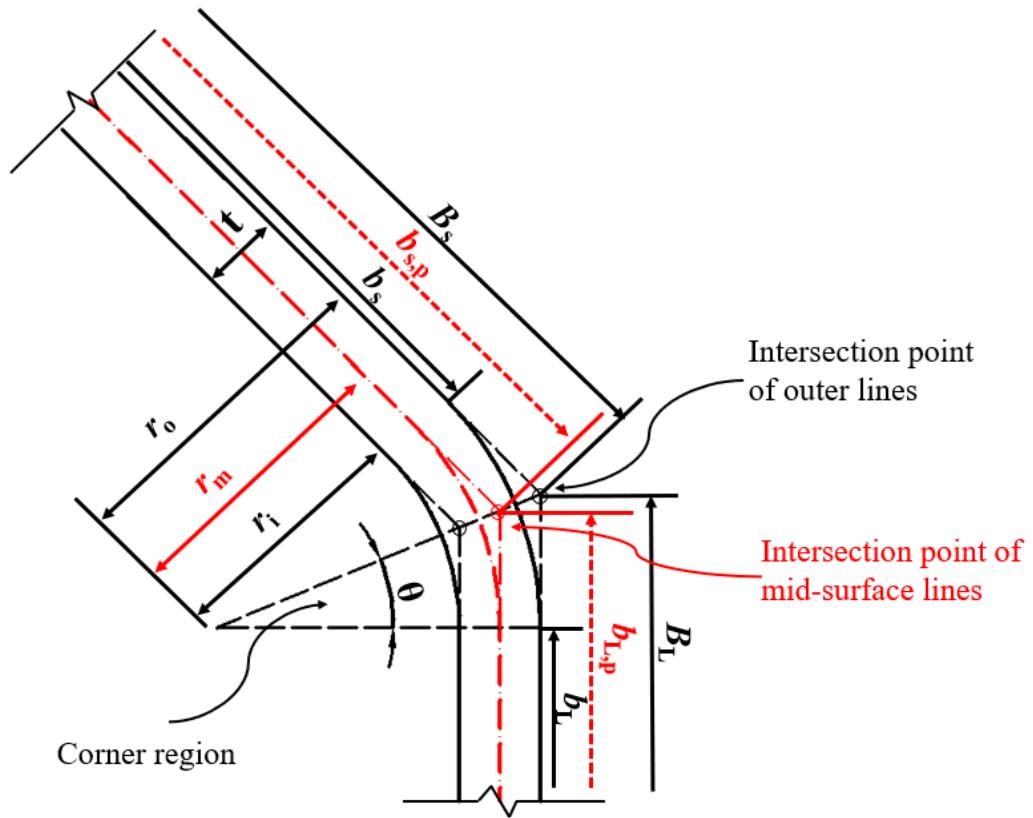
Fig. 3. Detailed geometry and definition of symbols.
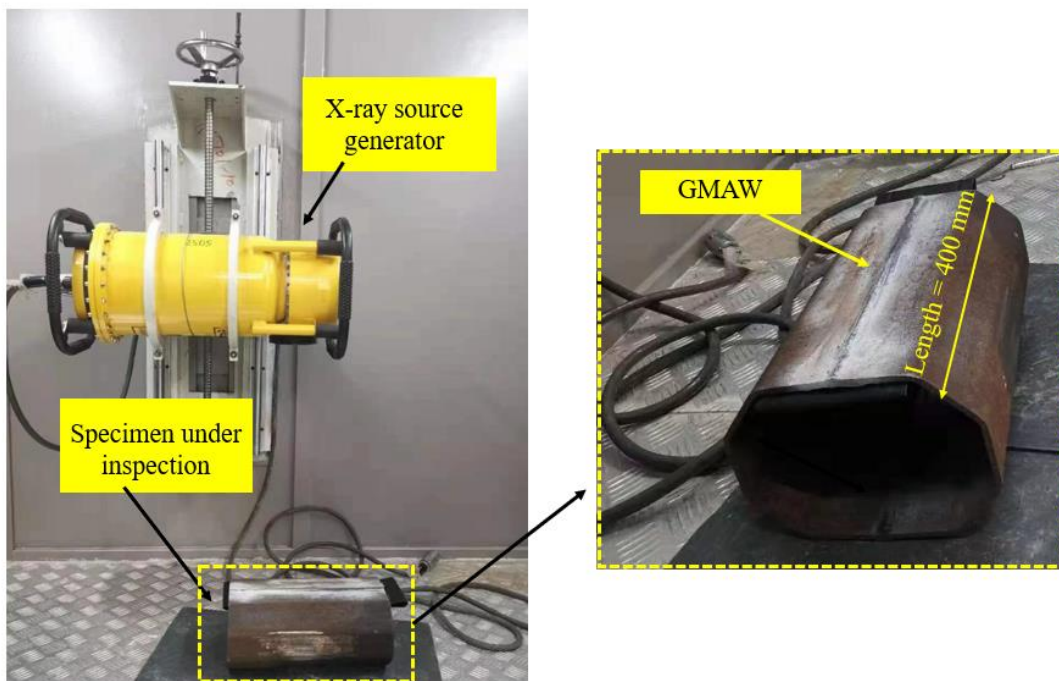
Fig. 4. Schematic view of the test set-up of the industrial X-ray inspection for the welding.
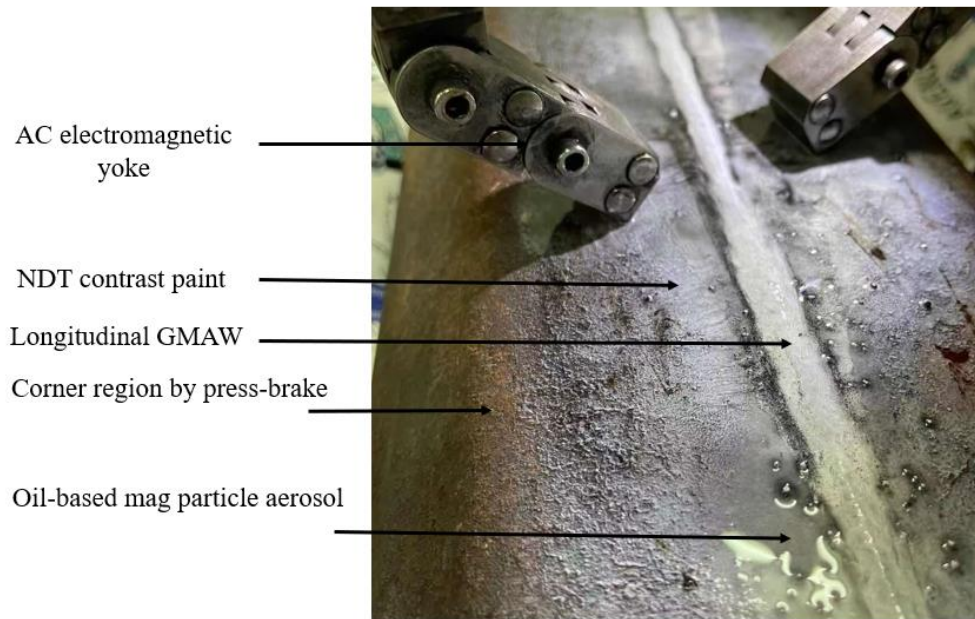
Fig. 5. Non-destructive inspection for corner region and welding surface (magnetic particles inspection).

(a)
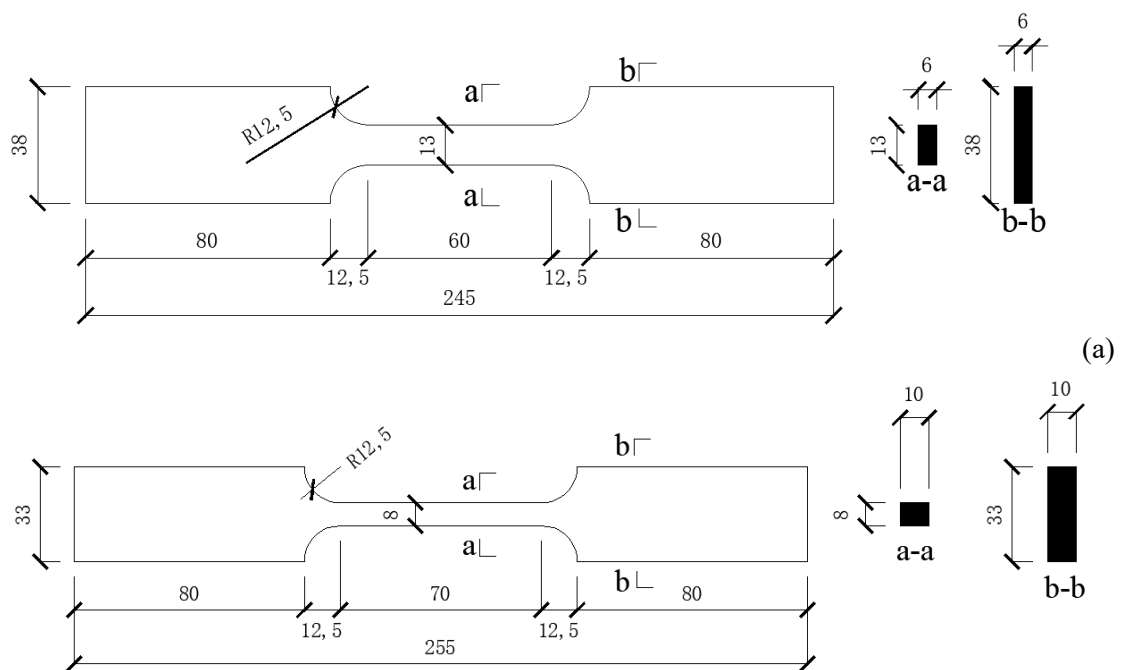
(b)

Fig. 6. Dimensions of flat coupon specimens taken from the parent steel plates, in mm (a) Flat coupon specimen taken from the 6 mm steel plate (b) Flat coupon specimen taken from the 10 mm steel plate.

(a)
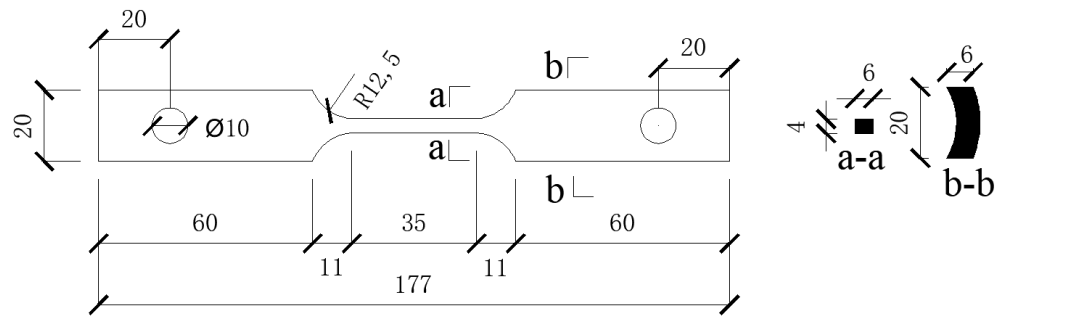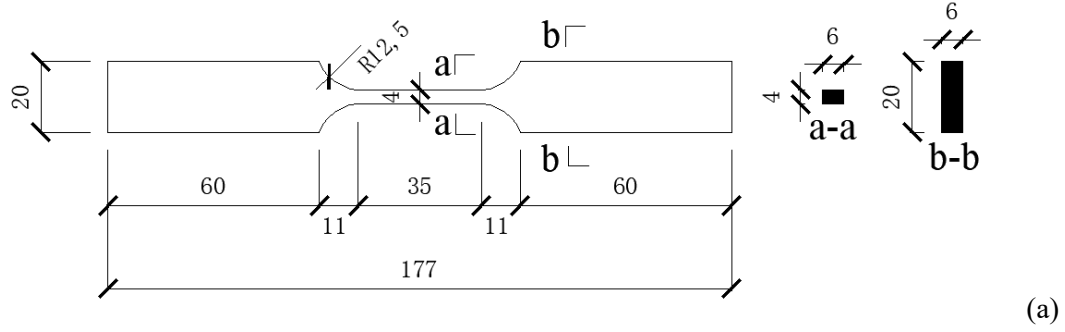
(b)

Fig. 7. Dimensions (in mm) of flat and corner coupon specimens taken within the cross section of HSS IOctHS with thickness of 6 mm (a) Flat coupon (b) Corner coupon.

(a)
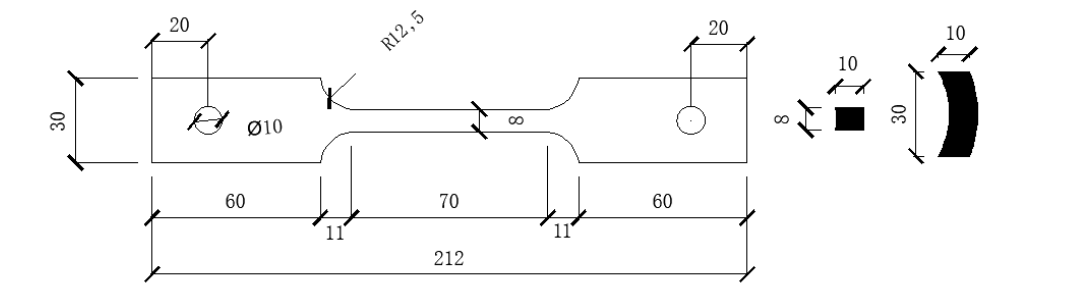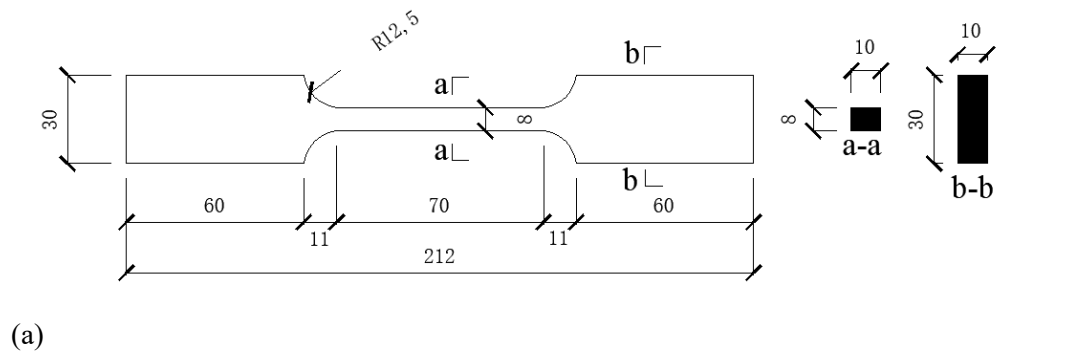
(b)

Fig. 8. Dimensions (in mm) of flat and corner coupon specimens taken within the cross section of HSS IOctHS with thickness of 10 mm (a) Flat coupon (b) Corner coupon.
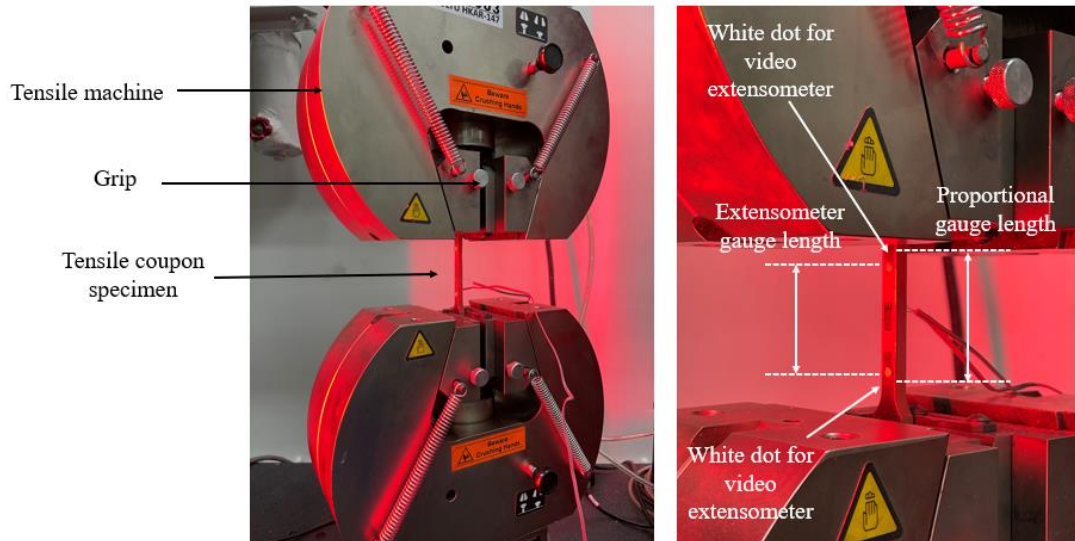
(a)
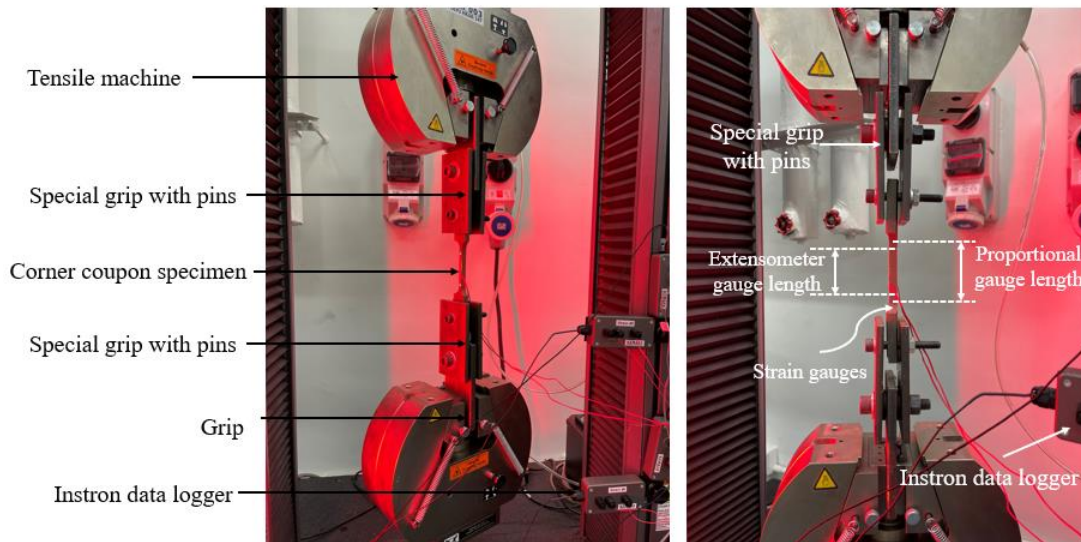
(b)

Fig. 9. Test set-up for tensile coupon tests (a) Test set-up for flat coupon specimens (b) Test set-up for corner coupon specimens.
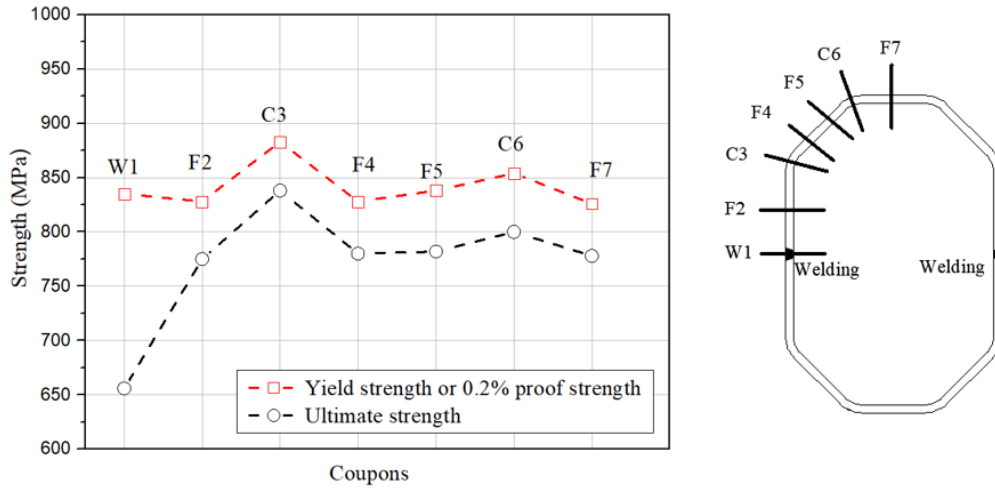
Fig. 10. Distribution of the yield strength or 0.2% proof strength and the ultimate strength within the section of IOctHS145×6-1.50.
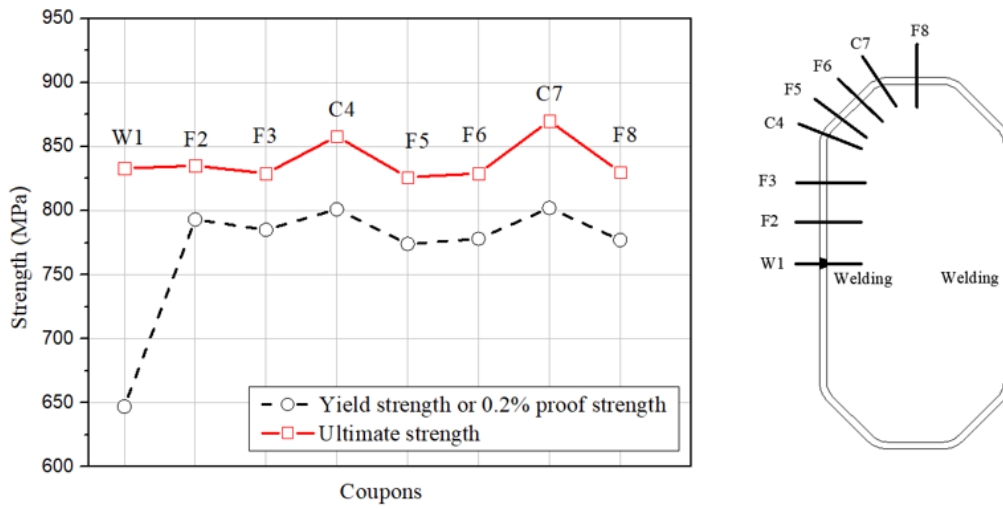
Fig. 11. Distribution of the yield strength or 0.2% proof strength and the ultimate strength within the section of IOctHS220×6-1.50.

6
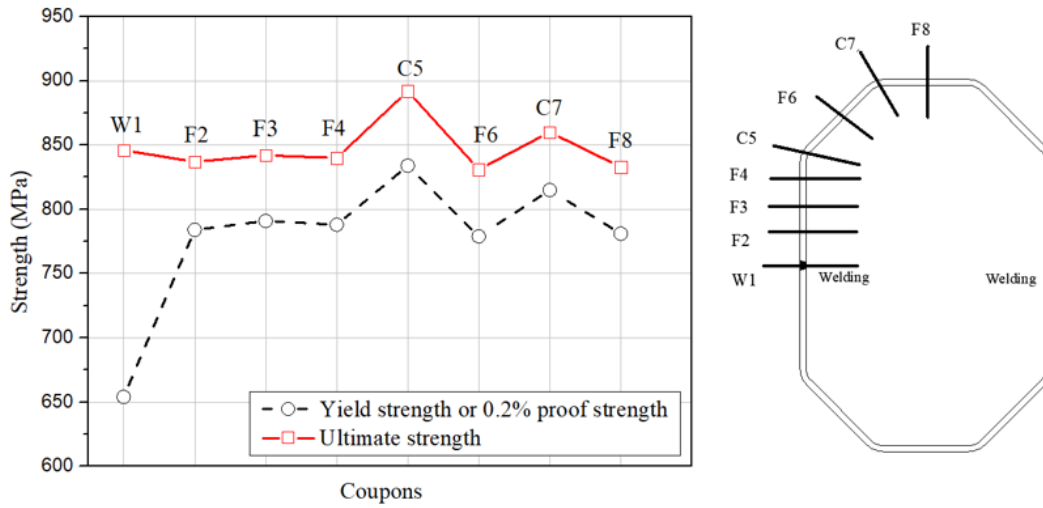
Fig. 12. Distribution of the yield strength or 0.2% proof strength and the ultimate strength within the section of IOctHS225×6-2.00.
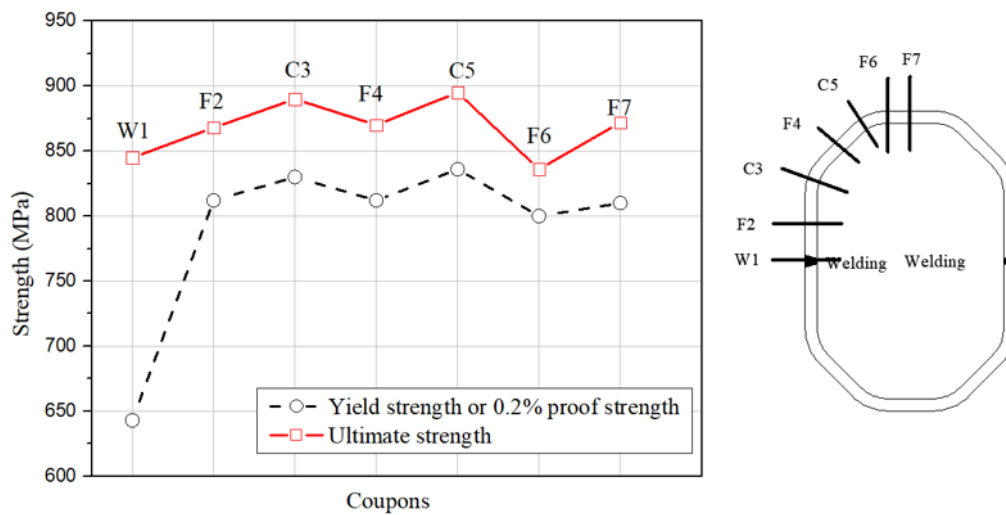
Fig. 13. Distribution of the yield strength or 0.2% proof strength and the ultimate strength within the section of IOctHS145×10-1.50.
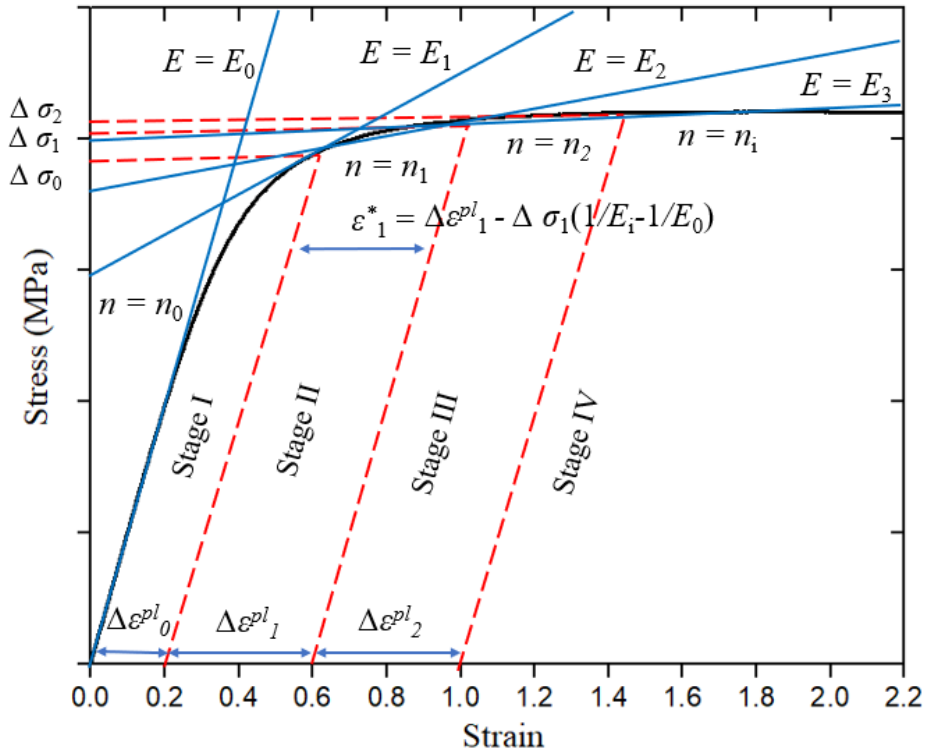
Fig. 14. Schematic view of the multi-stage stress-strain model.
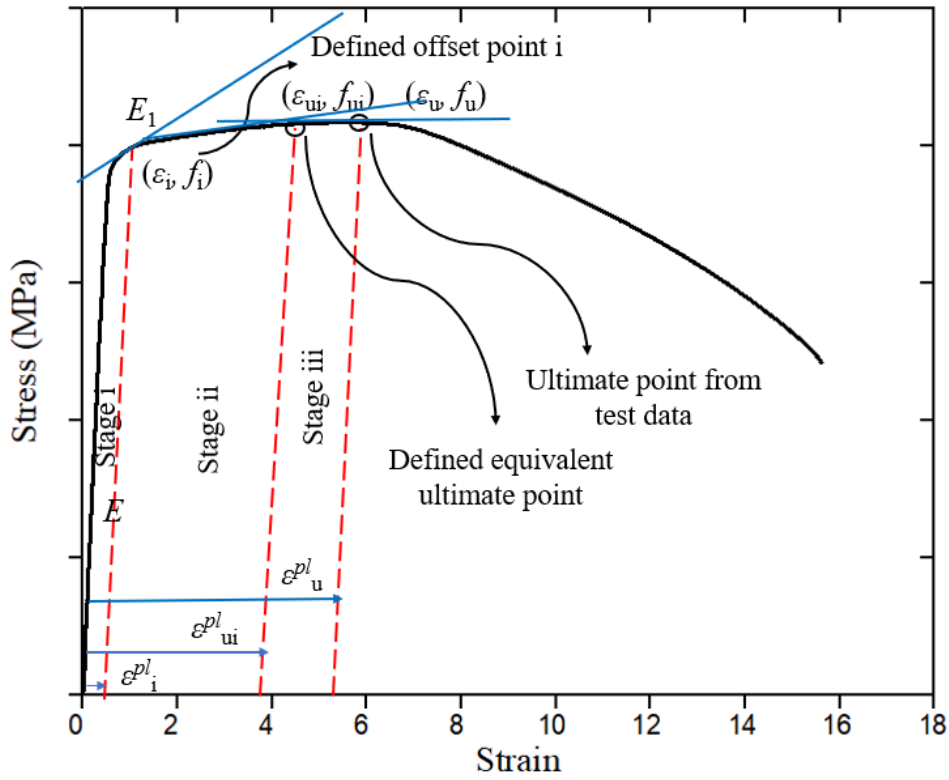
Fig. 15. Schematic view of the stress-strain model with an optimized offset yield point.
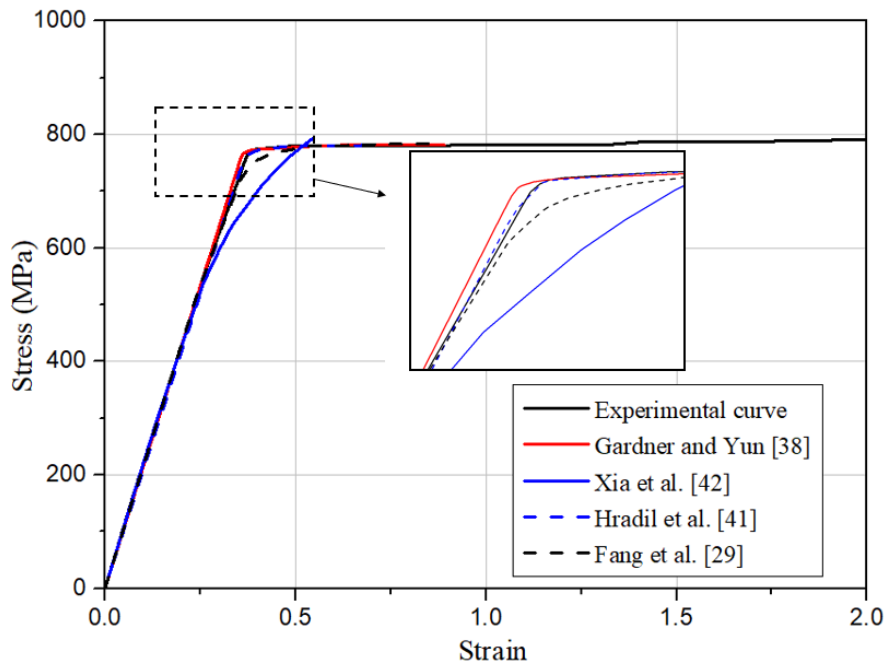
(a)
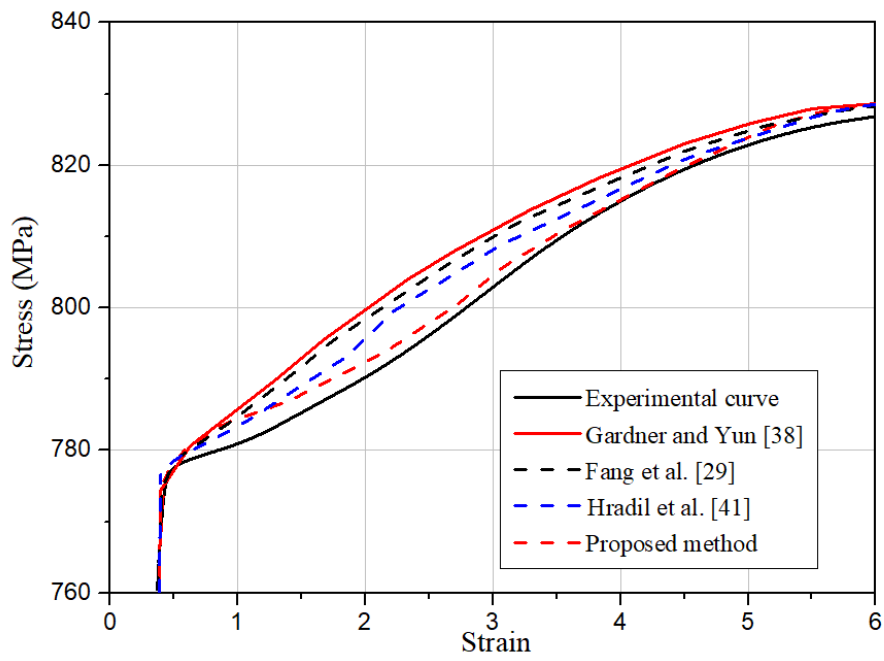
(b)
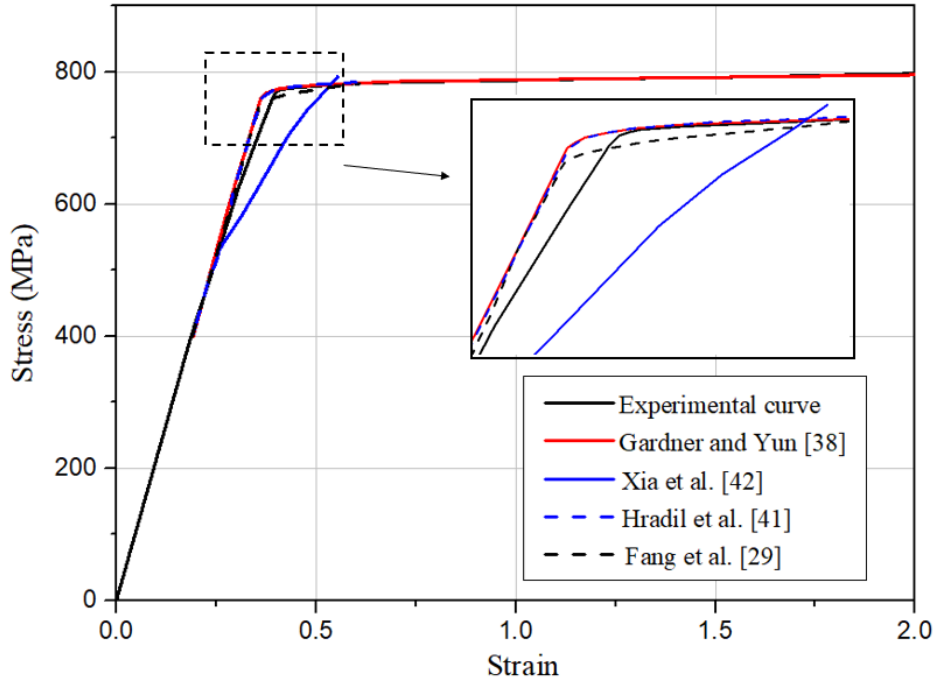
(c)
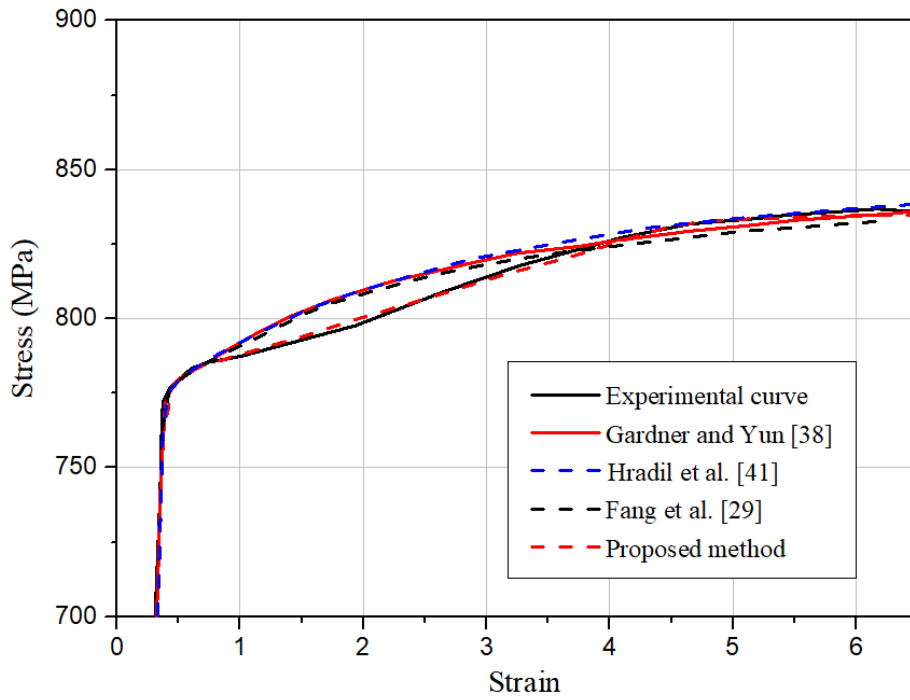
(d)

Fig. 16. Comparison of experimental stress-strain curves from flat coupon specimens with different predictive models (a) First stage of IOctHS145×6-1.50-F4 (b) Second stage of IOctHS145×6-1.50-F4 (c) First stage of IOctHS225×6-2.00-F6 (d) Second stage of IOctHS225×6-2.00-F6.
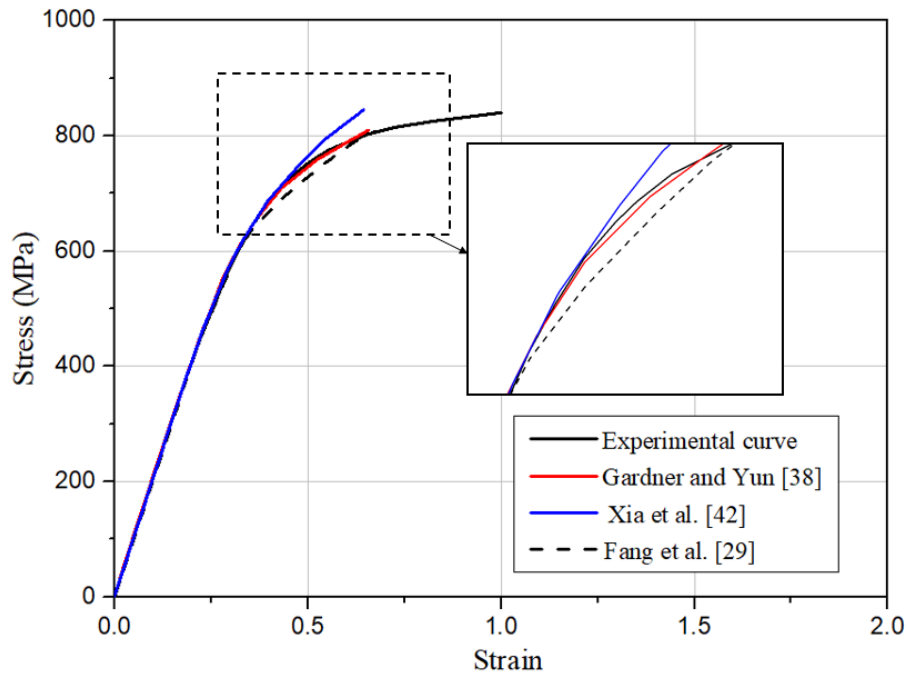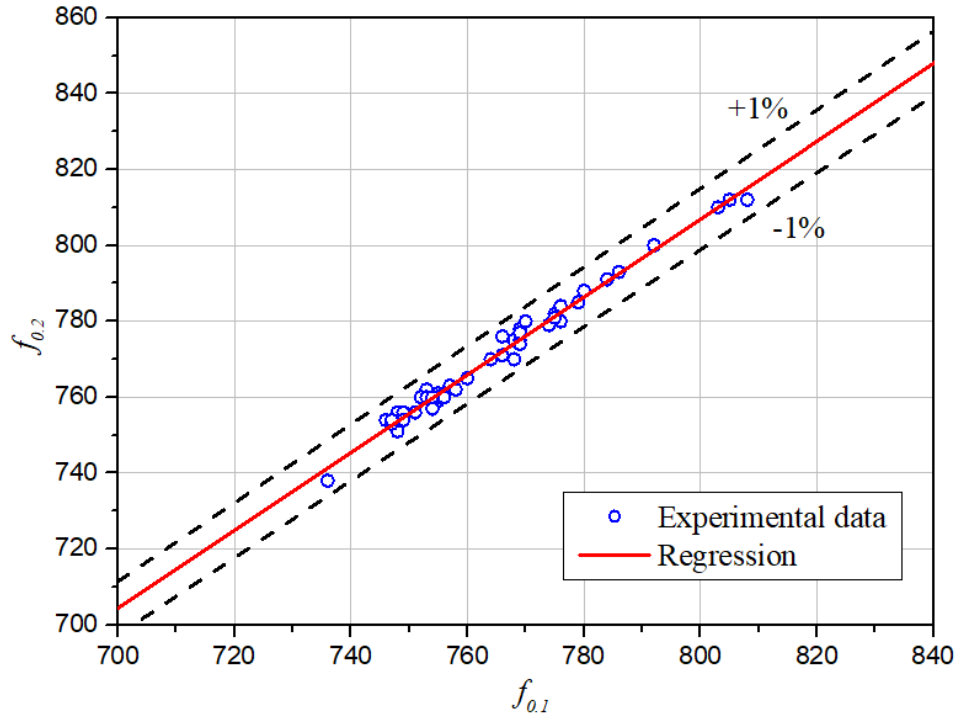
(a)
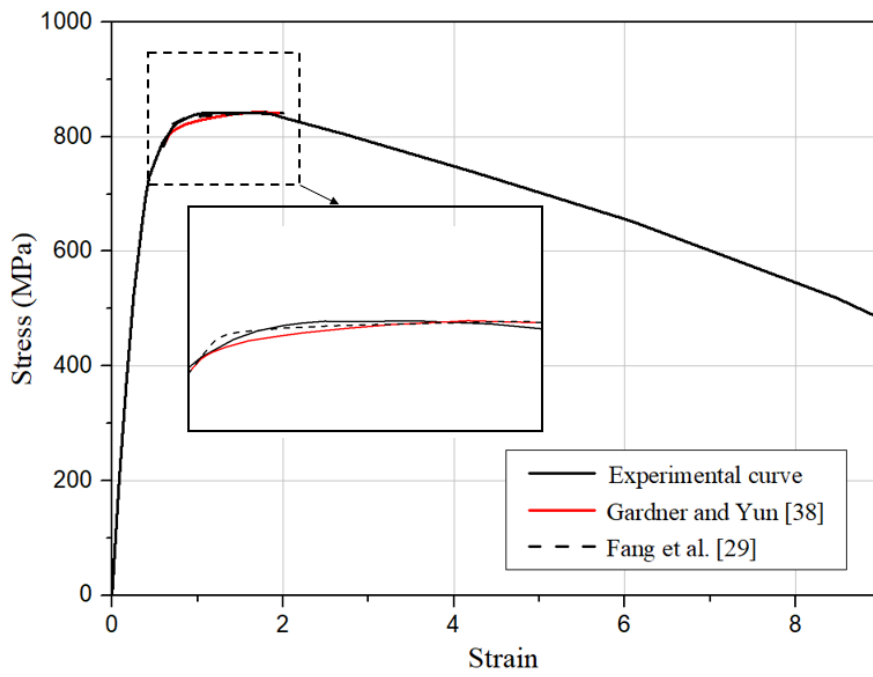
(b)
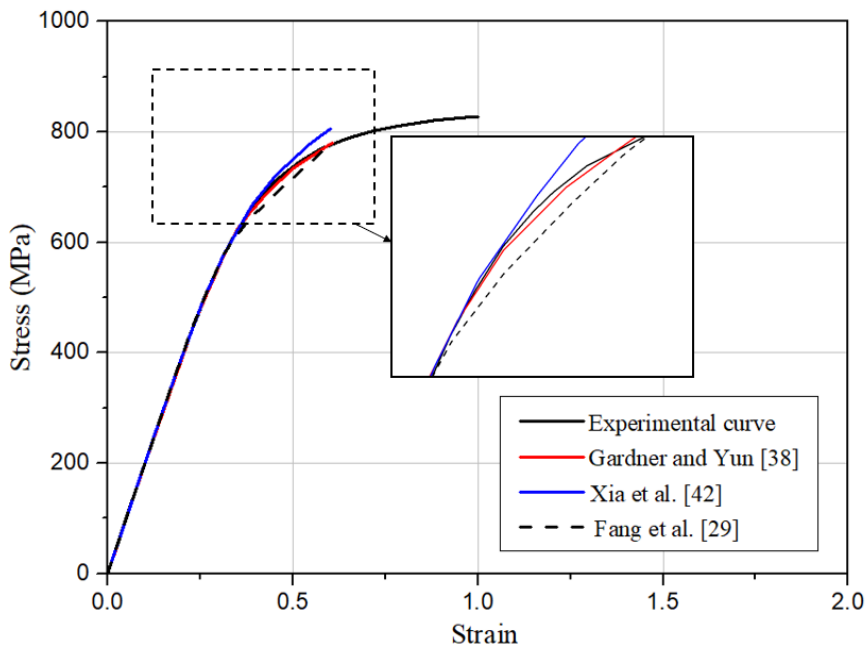
(c)
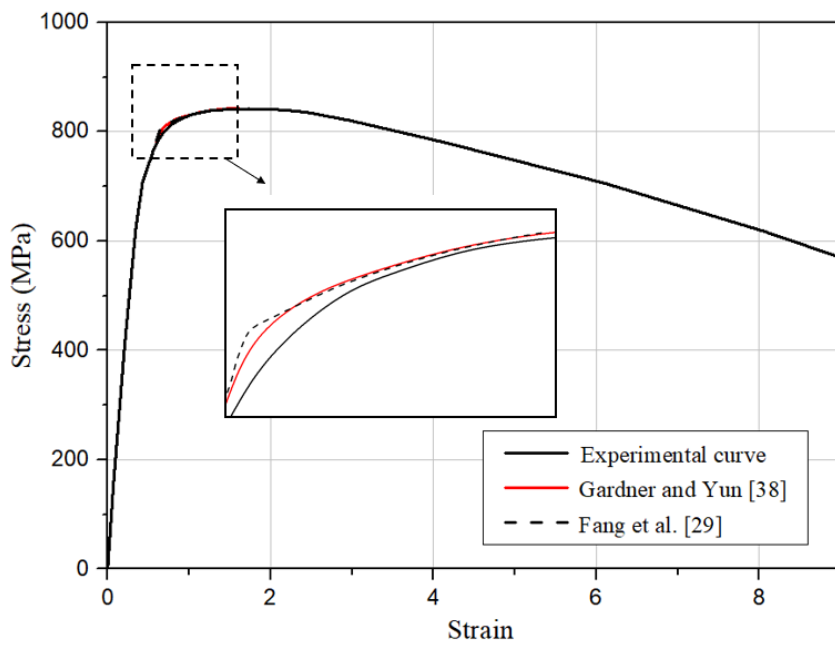
(d)

Fig. 17. Comparison of experimental stress-strain curves from corner coupon specimens with different predictive models (a) First stage of IOctHS145×6-1.50-C6 (b) Second stage of IOctHS145×6-1.50-C6 (c) First stage of IOctHS225×6-2.00-C7 (d) Second stage of IOctHS225×6-2.00-C7.

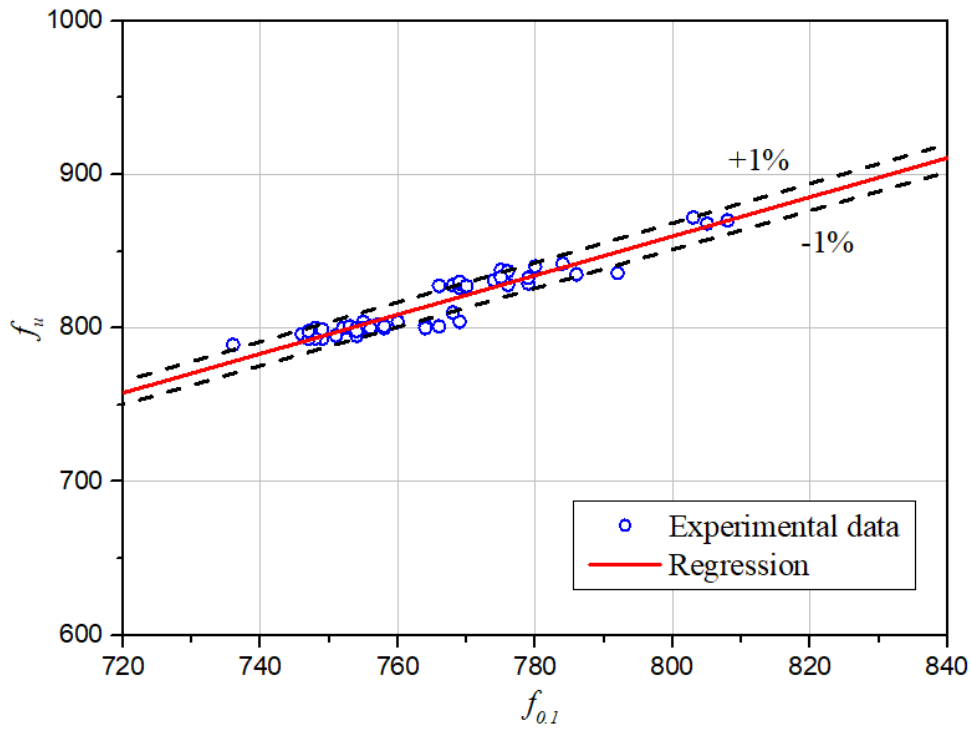Fig. 18. The relationship between the 0.2% proof strength and 0.1% proof strength.

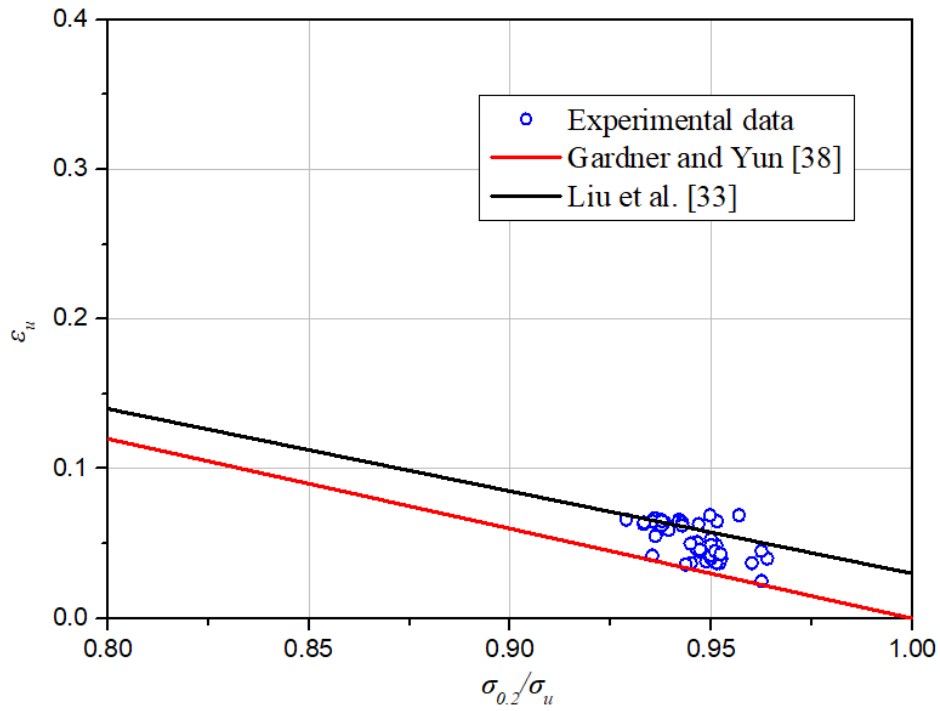Fig. 19. The relationship between the ultimate strength and 0.1% proof strength.

13

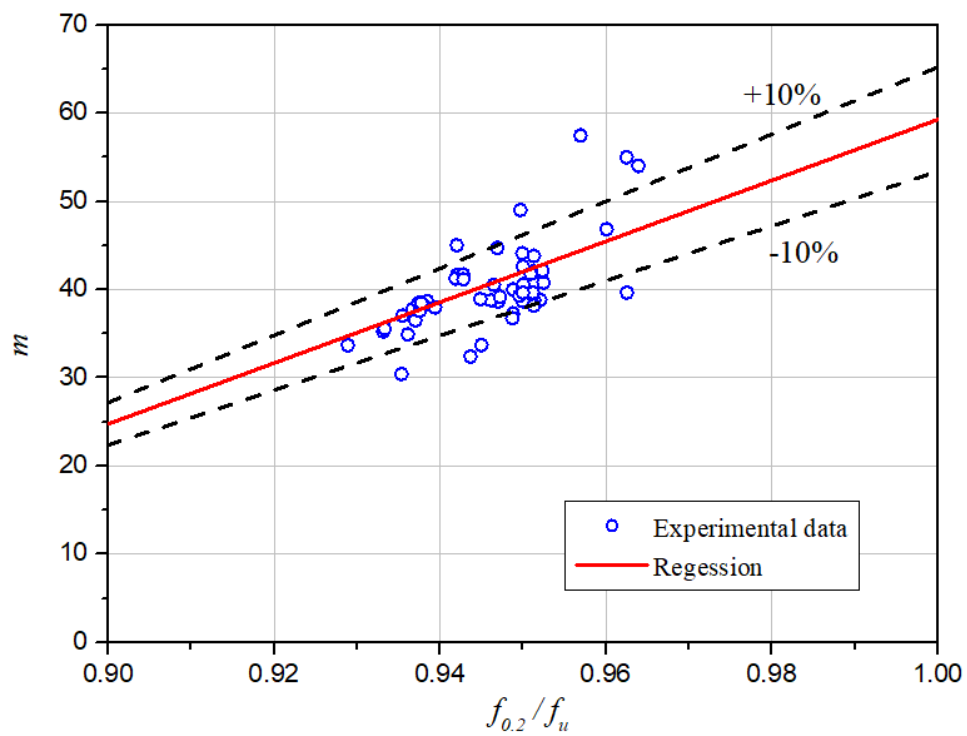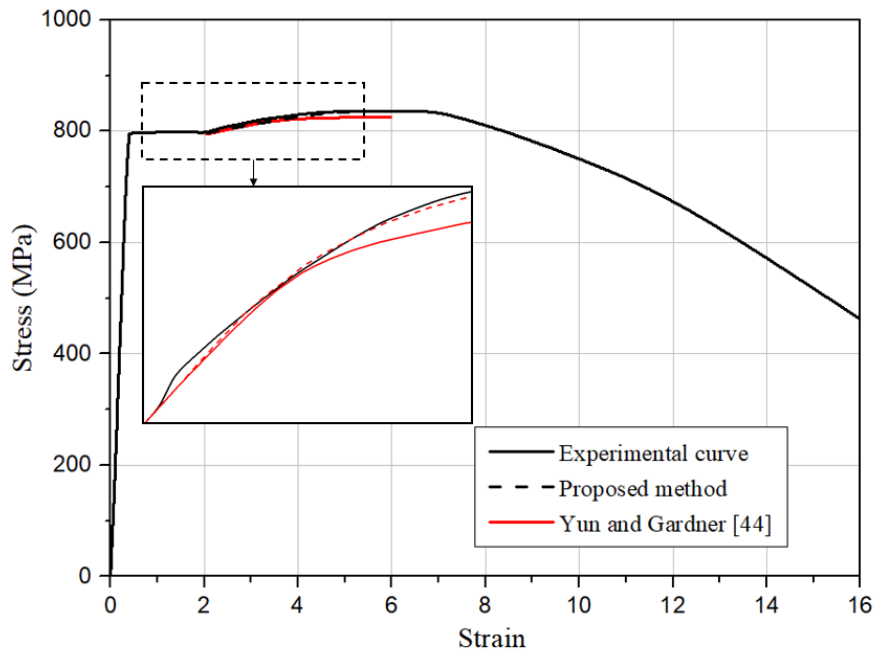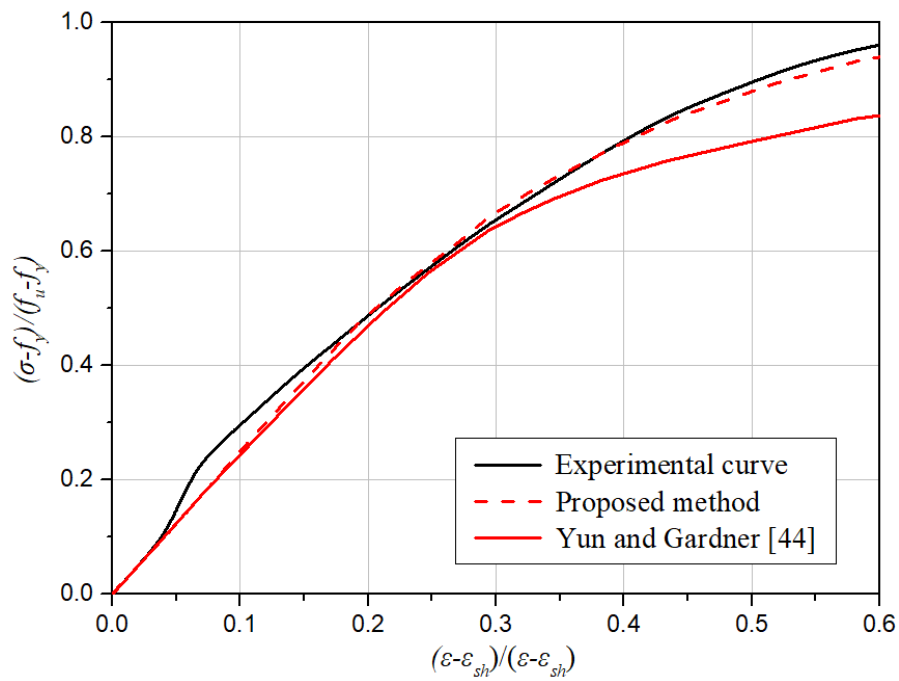Fig. 20. Comparison of the ultimate strain between experimental data and predictions.

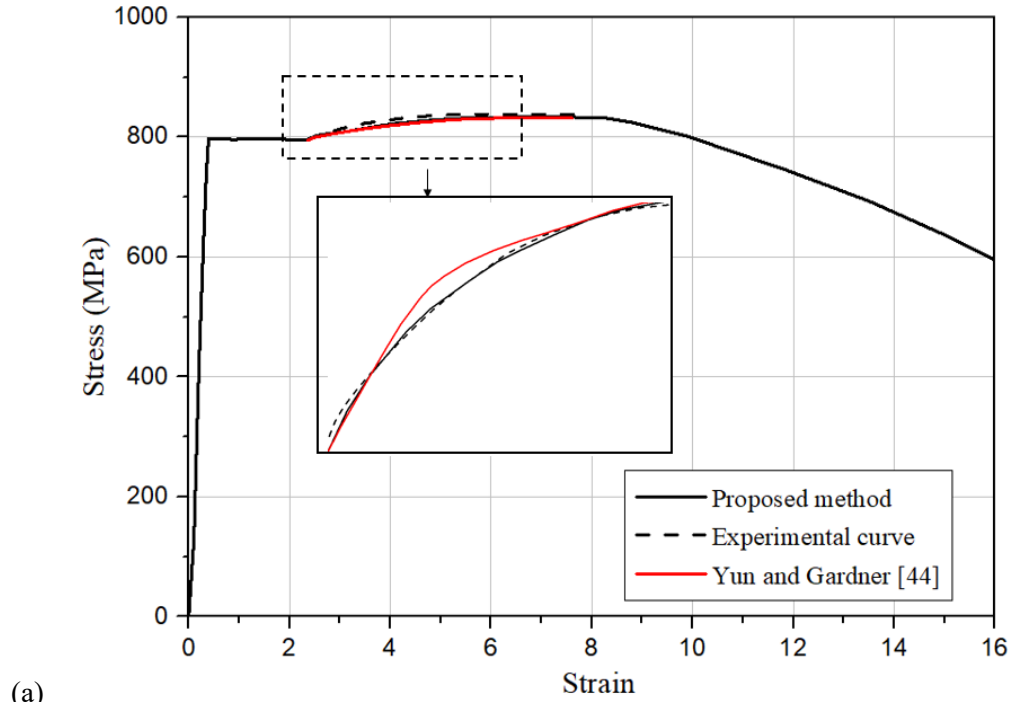Fig. 21. Predicted equation for exponential coefficient *m* of second stage.

(a)

(b)

Fig. 22. Comparison of experimental stress-strain curves with yeild plateau and predicitive model for IOctHS145×6-1.50-F2 (a) Full stress-strain curves (b) Strain hardening stage with normalized stress-stain relationship.
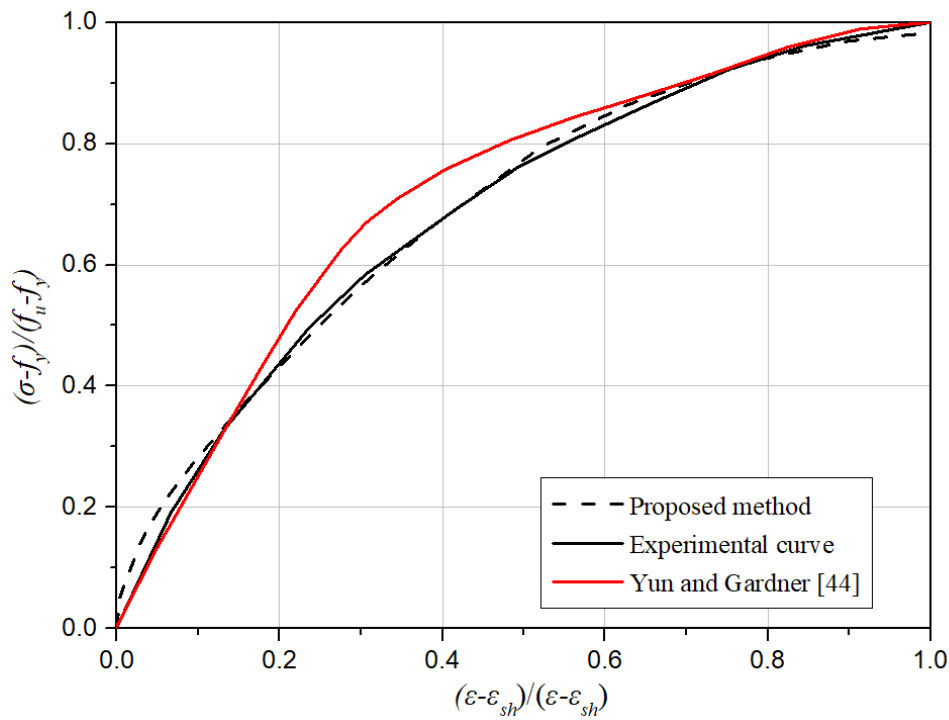
(a)

(b)

Fig. 23. Comparison of experimental stress-strain curves with yeild plateau and predicitive model for IOctHS145×10-1.50-F7 (a) Full stress-strain curves (b) Strain hardening stage with normalized stress-stain relationship.

(a)

(b)   (c)
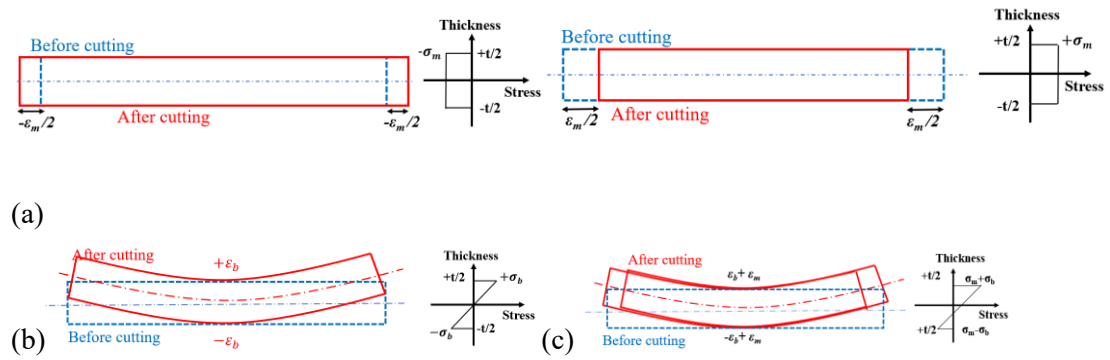
Fig.24. Effects of membrane and bending residual stresses (a) Membrane residual stress (b) Bending residual stress (c) Combined bending and tensile membrane residual stresses.

Fig. 25. Prepared IOctHS225×6-2.00 specimen with outer and inner electric strain gauges ready for the sectioning process.

Fig. 26. Sectioning process using wire-cutting with coolant.
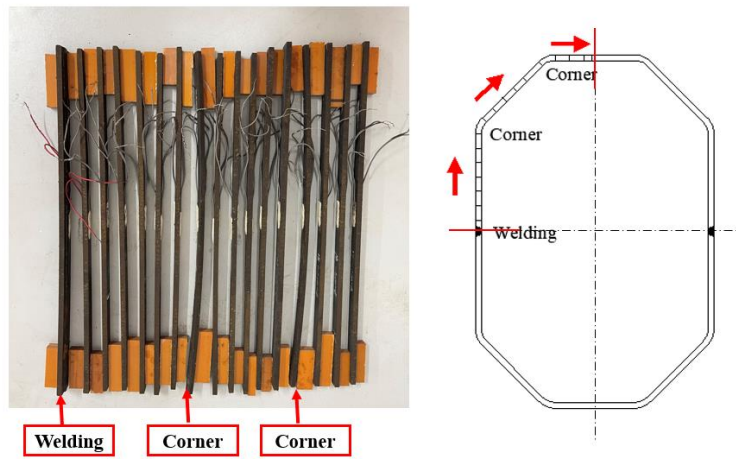
Fig. 27. Deformed strips extracted from IOctHS225×6-2.00 after sectioning process.
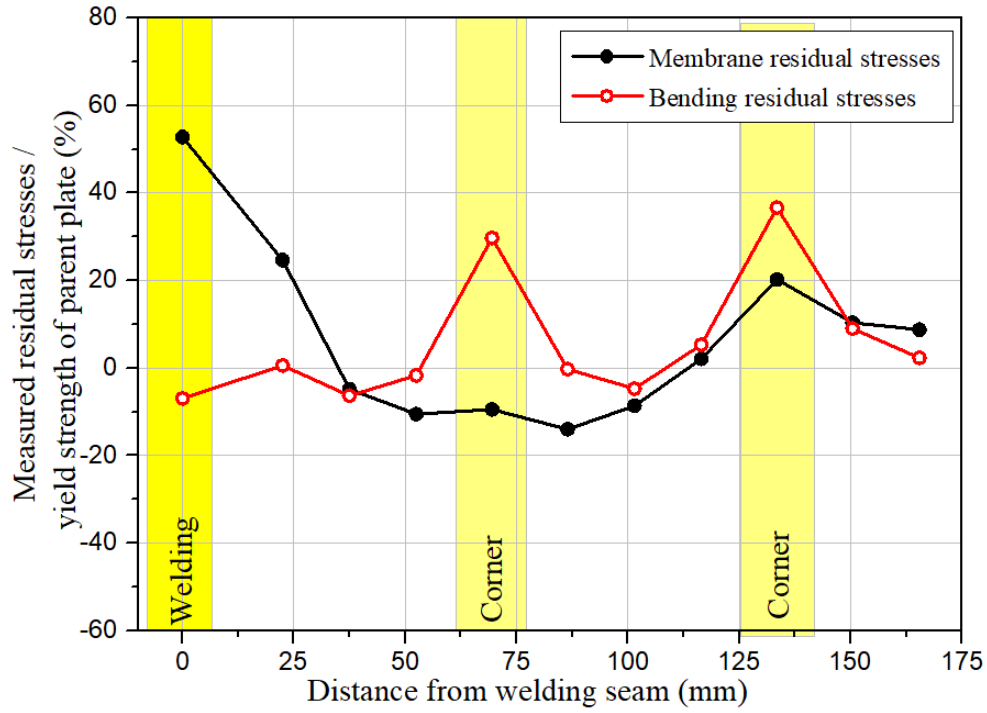
Fig. 28. Magnitude and the distribution of the longitudinal residual stresses in IOctHS145×6-1.50.
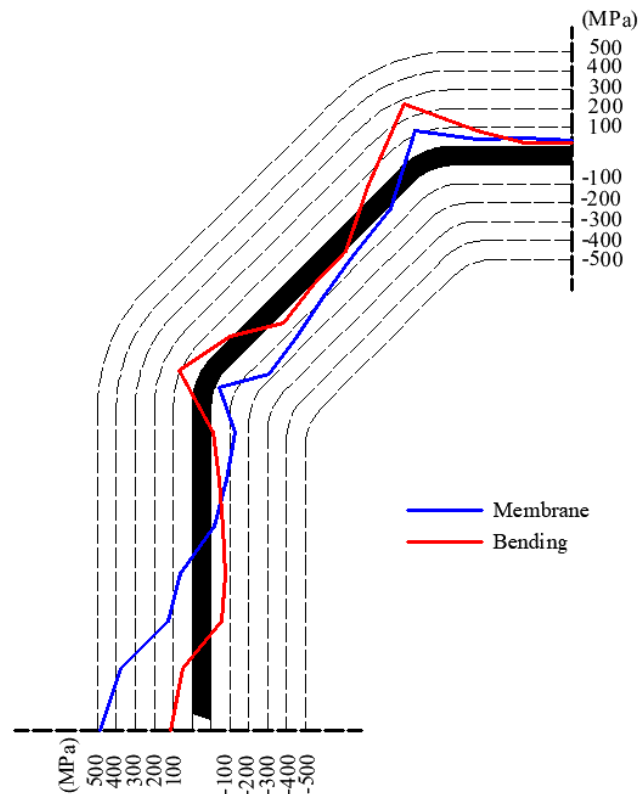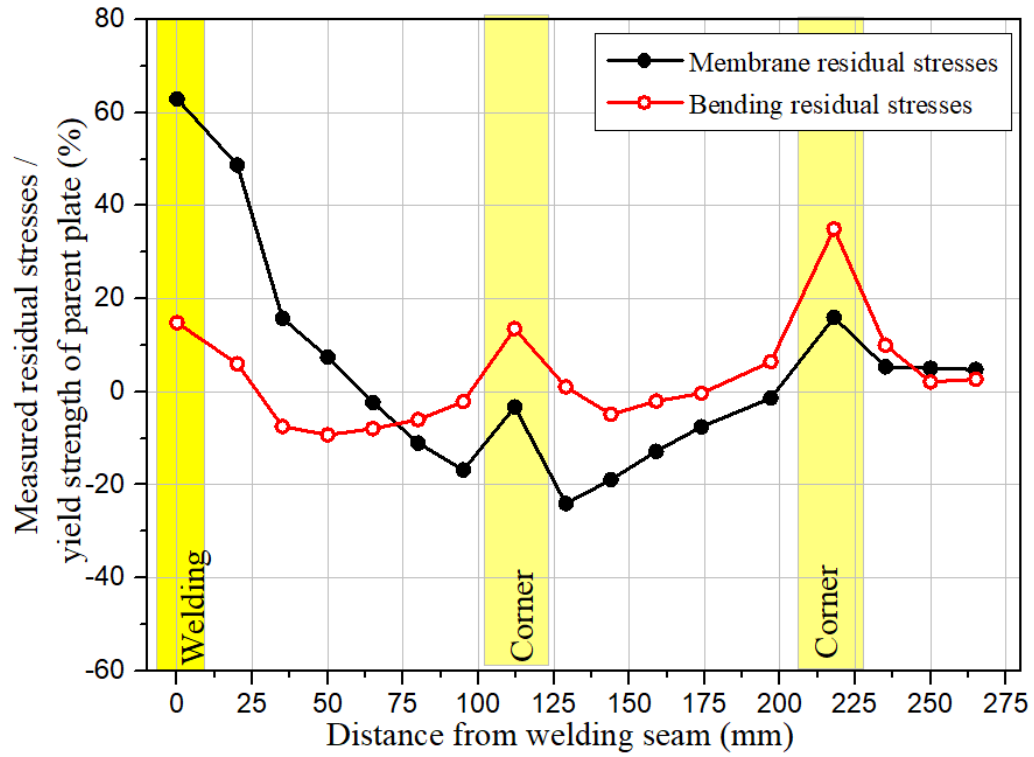
Fig. 29. Magnitude and the distribution of the longitudinal residual stresses in IOctHS220×6-1.50.
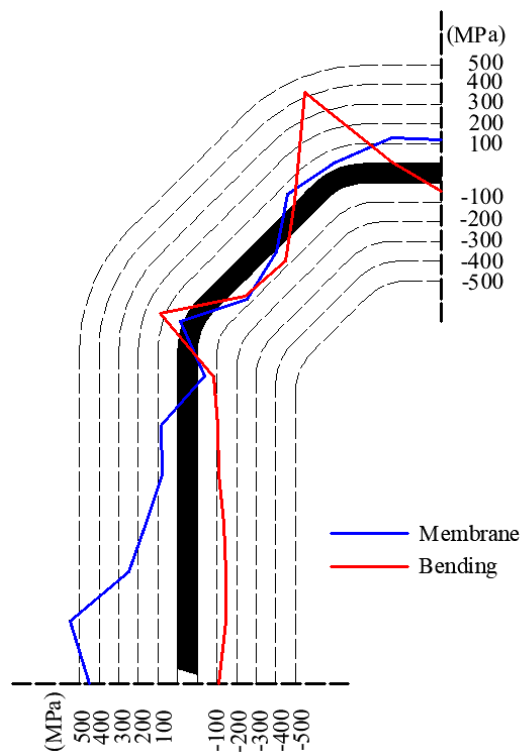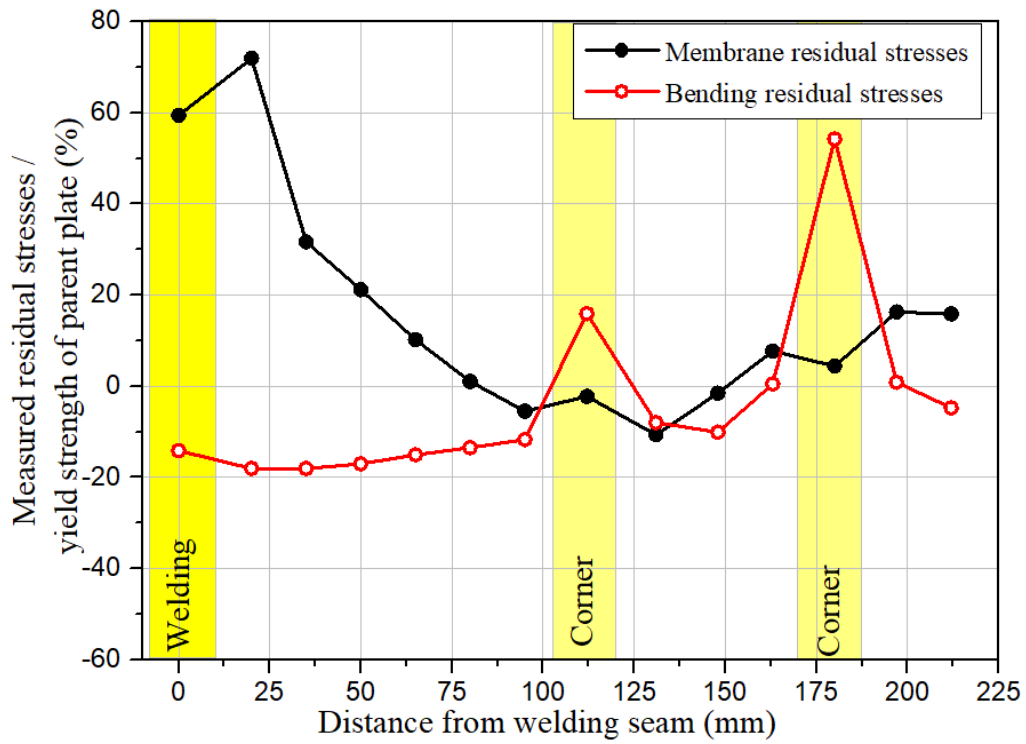
Fig. 30. Magnitude and the distribution of the longitudinal residual stresses in IOctHS225×6-2.00.
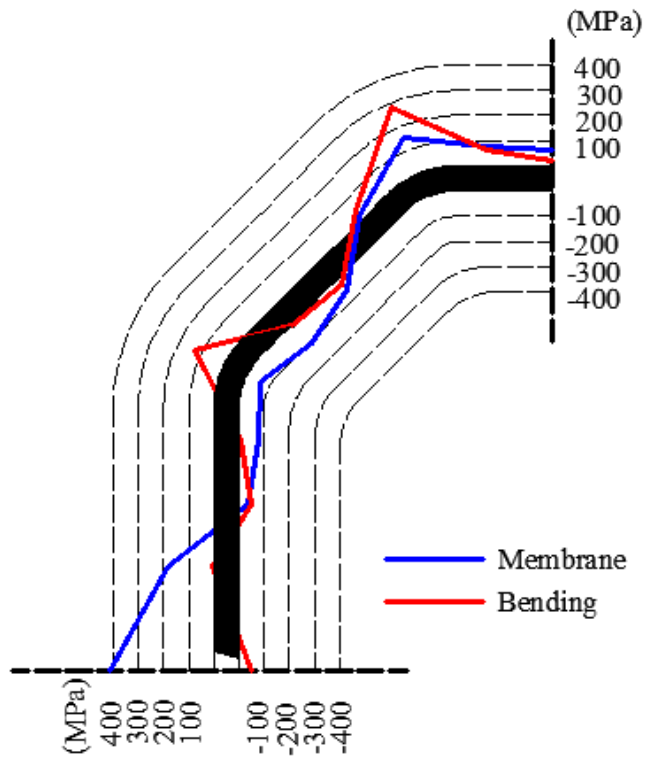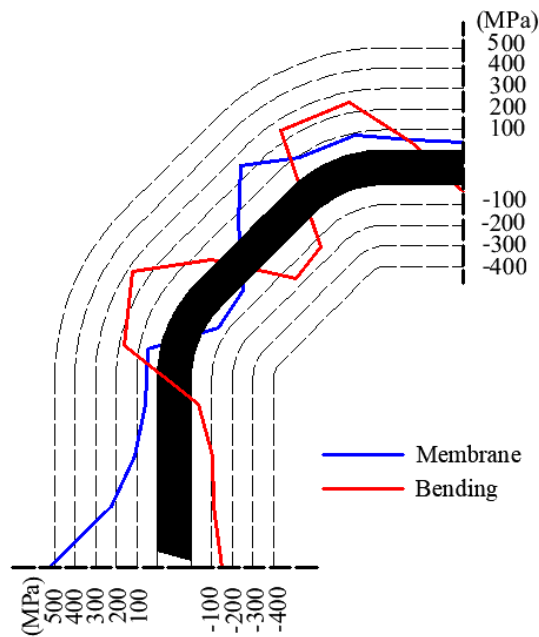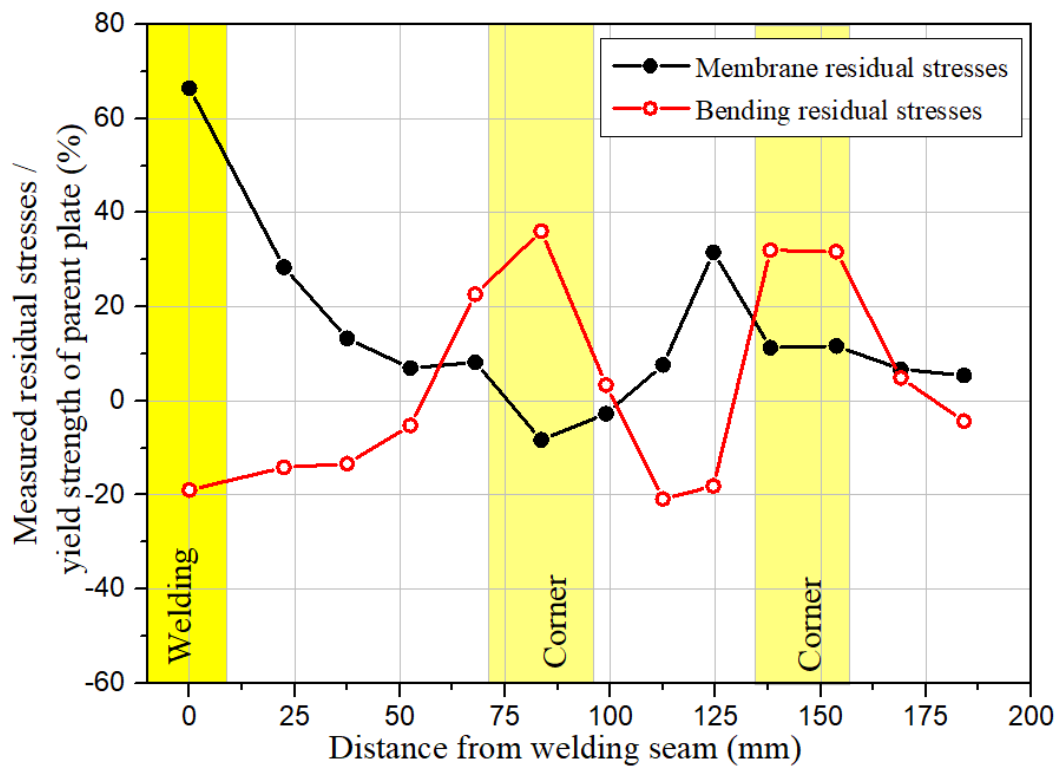
Fig. 31. Magnitude and the distribution of the longitudinal residual stresses in IOctHS145×10-1.50.
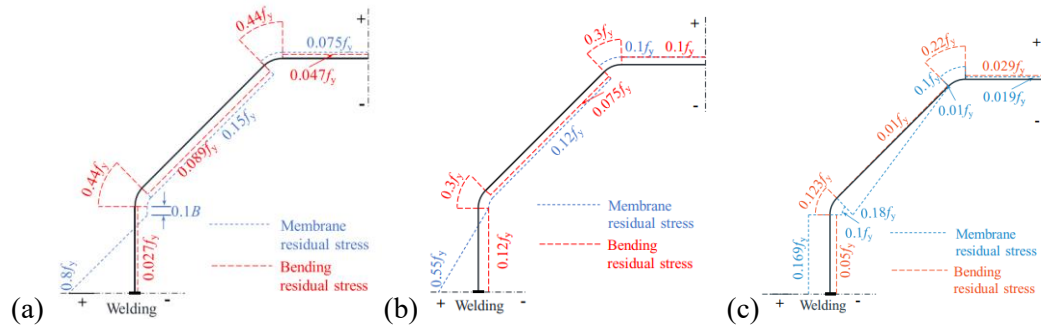
Fig. 32. Predictive model for cold-formed regular octagonal hollow sections with yield strength varying from S355, Q460 and Q690 (a) Predictive model in Zhu et al. [13] (b) Predictive model for residual stresses in octagonal hollow sections proposed by Chen et al. [19] (c) Predictive model for residual stresses in octagonal sections by Fang et al. [29].
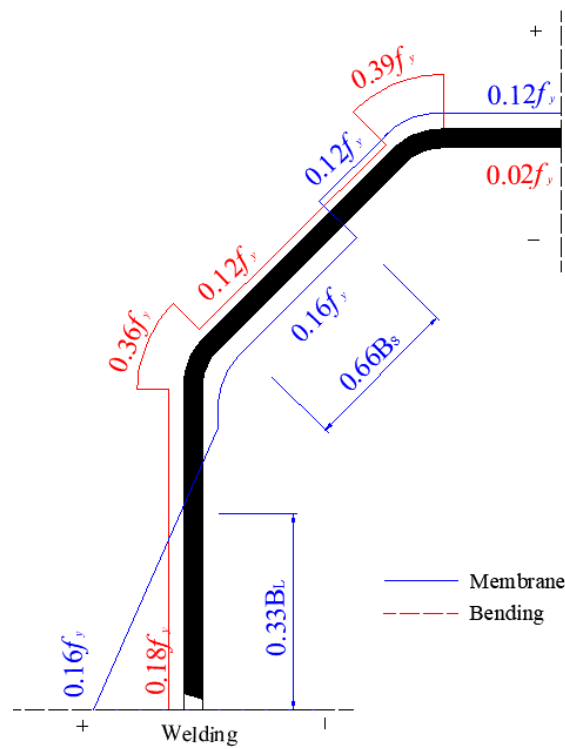
Fig. 33. Predictive model for residual stresses in HSS Q690 cold-formed irregular octagonal hollow sections.

Table 1 Chemical compositions listed in mill certificates for HSS plates.

Steel plate	Chemical composition (wt%)										
	C	Mn	P	S	Si	Cr	Mo	Nb	Ti	B	CEV
6 mm plate	0.13	1.39	0.011	0.001	0.26	0.27	0.14	0.027	0.015	0.002	0.45
10 mm plate	0.14	1.41	0.012	0.001	0.26	0.26	0.15	0.025	0.014	0.002	0.46
EN 10025-6 [49]	0.22	1.80	0.025	0.012	0.86	1.60	0.74	0.07	0.07	0.006	0.65

Table 2 Chemical compositions of the welding electrode ER110S-G.

Electrode	Chemical composition (wt%)										
	C	Mn	P	S	Si	Cr	Mo	Nb	Ti	V	Ni
ER110S-G	0.09	1.70	0.009	0.008	0.70	0.30	0.60	0.027	0.1	0.03	1.85

Table 3 Measured dimensions of cold-formed HSS irregular octagonal hollow section (IOctHS) specimens.

Specimens	Edge length B_s (mm)	Side width b_s (mm)	Edge length B_L (mm)	Side width b_L (mm)	Thickness t (mm)	Inner radius r_i (mm)
IOctHS145×6-1.50	66.5	46.5	144.4	124.5	5.9	18.1
IOctHS220×6-1.50	104.0	84.2	219.9	200.1	5.9	17.9
IOctHS225×6-2.00	67.6	54.6	224.4	204.5	5.9	17.9
IOctHS145×10-1.50	69.9	36.8	146.2	113.1	9.9	30.2

Table 4 Test results of the flat coupons taken from the HSS parent plates.

Section	$E_{s,p}$ (GPa)	v	$f_{y,p}$ (Mpa)	$f_{u,p}$ (Mpa)	$\varepsilon_{u,p}$ (%)	$\varepsilon_{f,p}$ (%)	$\varepsilon_{sh,p}$ (%)
6 mm plate	214.1	0.29	768.5	816.2	6.45	14.95	1.98
10 mm plate	216.1	0.30	791.3	825.6	6.55	16.18	2.32

Table 5 Test results of the material properties within the cold-formed section IOctHS145×6-1.50.

Section	E_s (GPa)	f_y (MPa)	f_u (MPa)	ε_u (%)	$\varepsilon_{f,25ex}$ (%)	ε_f (%)	ε_{sh} (%)	$f_{0.05}$ (MPa)	$f_{0.1}$ (MPa)	n
IOctHS145×6-1.50-W1	178.5	656	835	8.5	19.2	18.8	-*	-^	-Δ	-^
IOctHS145×6-1.50-F2	202.8	775	828	6.7	16.2	16.5	1.95	-^	-Δ	-^
IOctHS145×6-1.50-C3	199.2	832	883	1.6	12.6	11.9	-*	766	803	17
IOctHS145×6-1.50-F4	214.3	780	828	6.6	17.8	17.2	-*	776	778	267
IOctHS145×6-1.50-F5	212.1	782	838	6.3	14.5	16.2	-*	775	779	154
IOctHS145×6-1.50-C6	196.7	800	854	1.9	12.7	12.4	-*	720	767	13
IOctHS145×6-1.50-F7	213.6	778	826	6.5	16.8	16.5	-*	772	775	179

Note: * indicates the strain hardening was not observed from the tensile coupon test. ^ indicates that the 0.05% proof strength and strain hardening parameter are not applicable to the welding materials coupon or coupon with yield plateau. Δ indicates that 0.1% proof strength is not applicable to the welding materials coupon or coupon with yield plateau.

Table 6 Test results of the material properties within the cold-formed section IOctHS220×6-1.50.

Section	E_s (GPa)	f_y (MPa)	f_u (MPa)	ε_u (%)	$\varepsilon_{f,25ex}$ (%)	ε_f (%)	ε_{sh} (%)	$f_{0.05}$ (MPa)	$f_{0.1}$ (MPa)	n
IOctHS220×6-1.50-W1	171.2	647	833	8.8	17.9	18.5	-*	-^	-Δ	-^
IOctHS220×6-1.50-F2	215.2	793	835	6.9	-#	17.5	1.88	-^	-Δ	-^
IOctHS220×6-1.50-F3	206.5	785	829	6.3	-#	16.8	-*	781	786	271
IOctHS220×6-1.50-C4	199.7	801	858	1.8	12.4	13.2	-*	746	780	19
IOctHS220×6-1.50-F5	208.8	774	826	5.9	15.9	16.4	-*	765	776	119
IOctHS220×6-1.50-F6	206.5	778	829	6.4	17.4	17.1	-*	773	776	215
IOctHS220×6-1.50-C7	201.2	802	870	2.0	13.7	13.2	-*	730	771	15
IOctHS220×6-1.50-F8	214.2	777	830	5.5	15.8	16.1	-*	758	770	56

Note: # indicates the occurrence of the fracture is located outside the range of the extensometer gauge length. * indicates the strain hardening was not observed from the tensile coupon test. ^ indicates that the 0.05% proof strength and strain hardening parameter are not applicable to the welding materials coupon or coupon with yield plateau. Δ indicates that 0.1% proof strength is not applicable to the welding materials coupon or coupon with yield plateau.

Table 7 Test results of the material properties within the cold-formed section IOctHS225×6-2.00.

Section	E_s (GPa)	f_y (MPa)	f_u (MPa)	ε_u (%)	$\varepsilon_{f,25ex}$ (%)	ε_f (%)	ε_{sh} (%)	$f_{0.05}$ (MPa)	$f_{0.1}$ (MPa)	n
IOctHS225×6-2.00-W1	178.3	654	846	10.5	18.3	18.5	-*	-^	-△	-^
IOctHS225×6-2.00-F2	205.5	784	837	6.5	16.9	17.1	-*	775	781	362
IOctHS225×6-2.00-F3	203.6	791	842	5.9	-#	16.2	-*	772	788	365
IOctHS225×6-2.00-F4	202.5	788	840	6.3	-#	15.7	-*	768	786	546
IOctHS225×6-2.00-C5	194.8	834	892	1.6	10.4	10.8	-*	750	802	35
IOctHS225×6-2.00-F6	206.4	779	831	6.6	16.3	16.2	-*	771	777	539
IOctHS225×6-2.00-C7	195.5	815	860	1.4	11.2	11.5	-*	765	797	62
IOctHS225×6-2.00-F8	210.2	781	833	6.2	16.6	16.3	-*	768	778	360

Note: * indicates the strain hardening was not observed from the tensile coupon test. ^ indicates that the 0.05% proof strength and strain hardening parameter are not applicable to the welding materials coupon or coupon with yield plateau. △ indicates that 0.1% proof strength is not applicable to the welding materials coupon or coupon with yield plateau.

Table 8 Test results of the material properties within the cold-formed section IOctHS145×10-1.50.

Section	E_s (GPa)	f_y (MPa)	f_u (MPa)	ε_u (%)	$\varepsilon_{f,50ex}$ (%)	ε_f (%)	ε_{sh} (%)	$f_{0.05}$ (MPa)	$f_{0.1}$ (MPa)	n
IOctHS145×10-1.50-W1	177.8	643	845	7.9	20.1	19.8	-*	-^	-△	-^
IOctHS145×10-1.50-F2	216.5	812	868	6.5	18.7	18.2	2.36	-^	-△	-^
IOctHS145×10-1.50-C3	213.3	830	890	1.8	12.6	12.2	-*	718	792	10
IOctHS145×10-1.50-F4	218.6	812	870	6.4	16.6	16.3	1.92	-^	-△	-^
IOctHS145×10-1.50-C5	212.3	836	895	1.7	11.8	12.1	-*	724	798	10
IOctHS145×10-1.50-F6	217.5	800	836	6.9	18.9	18.2	2.35	-^	-△	-^
IOctHS145×10-1.50-F7	219.2	810	872	6.6	18.3	17.6	2.41	-^	-△	-^

Note: # indicates the occurrence of the fracture is located outside the range of the extensometer gauge length. * indicates the strain hardening was not observed from the tensile coupon test. ^ indicates that the 0.05% proof strength and strain hardening parameter are not applicable to the welding materials coupon or coupon with yield plateau. △ indicates that 0.1% proof strength is not applicable to the welding materials coupon or coupon with yield plateau.

Table 9 Summary of the residual stress investigation for high strength steel.

Investigations	f_y (N/mm^2)	Cross section	Measurement method
Lee et al. [50]	690	plate-to-plate joint	hole-drilling
Wang et al. [51]	460	box section	sectioning
Ban et al. [52]	460	box section	sectioning
Ban et al. [53]	460	I-section	sectioning
Lee et al. [54]	690	T-joint	hole-drilling
Li et al. [55]	690	box and H-section	sectioning
Ma et al. [1]	460, 700 and 1100	CHS, RHS and SHS	sectioning
Khan et al. [56]	690	box section	neutron diffraction
Yang et al. [57]	690	box section	sectioning
Somodi and Kövesdi [6]	420 to 960	SHS	sectioning
Somodi and Kövesdi [28]	235 to 960	box section	sectioning
Liu and Chung [58]	690	H-section	hole-drilling
Fang et al. [29]	690	OctHS	sectioning
Sun et al. [59]	690	I-section	sectioning
Chen and Chan [19]	460	OctHS	sectioning
Chen and Chan [60]	460, 690 and 960	CHS	sectioning
Hu et al. [45]	690	CHS	sectioning
Su et al. [62]	690	I-section	sectioning
Su et al. [63]	960	I-section	sectioning